Universität Stuttgart

Improvement of the frictional contact algorithm
with application of pile installation

Shreyas Giridharan

IGS

Die Masterthesis wurde vom Kandidaten selbstständig, aber unter Anleitung des Betreuers erstellt. Sie ist nicht in allen Teilen geprüft.

Die Masterthesis ist Eigentum des IGS und sie darf deswegen nur mit dem Einverständnis des IGS ausgeliehen und kopiert (auch auszugsweise) werden.

Erklärung:

Hiermit erkläre ich, dass ich die vorliegende Arbeit selbstständig unter der Anleitung des Betreuers erarbeitet und dabei nur die angegebenen Quellen und Hilfsmittel verwendet habe.

Stuttgart, den 02.11.2016 _____

Shreyas Giridharan, Matrikelnummer: 2997069

Improvement of the frictional contact algorithm with application of pile installation

Fakultät für Bau– und Umweltingenieurwissenschaften

Universität Stuttgart

Masterthesis

vorgelegt von

Shreyas Giridharan

aus Chennai, Indien

Institutsleitung: Univ.-Prof. Dr.-Ing. habil. Christian Moormann

Betreuer: Dr.-Ing. Fursan Hamad

Abgabe: 31. Oct 2016

Institut für Geotechnik der Universität Stuttgart

2016

Abstract

Since the advent of finite element method, simulating practical applications and improving its accuracy has been of great interest in both the industry and academia. In recent years, tremendous progress has been achieved in applying the finite element method to a wide array of problems. Geomechanical simulation, owing to large deformations that happen during the course of simulation, which the traditional FE method cannot simulate well, needs more novel simulation methods. Additionally, the condition of non-penetration imposed by the FE method makes it difficult to simulate application like pile installation.

Material Point Method (MPM) has been developed combining the best features of both the Lagrangian and Eulerian methods, where the continuum is represented by particles called material points, which flow through the background computational mesh in a Eulerian fashion. MPM has been further developed to reduce the variations in internal force when the particles cross the cell boundary, to new versions like Generalised Interpolation Material Point method (GIMP) and Convected Particle Domain Interpolation method (CPDI).

In the present work, advanced version of MPM, the CPDI algorithm is used to model the behaviour of the bodies. An explicit Euler forward MPM scheme is used in the integration of this model. The boundary of the continuum is discretised separately from the MPM discretisation, and is traced accurately during the advancement of solution. A penalty function method, commonly used in Lagrangian analysis is used for evaluation of contact forces developed on the boundary. These contact forces are mapped to the computational mesh, where the momentum equation is solved, with the contact force as an external force. A fully drained hypoplastic sand model including stiffness anisotropy is used to simulate the behaviour of soil under dynamic loading. Finally, numerical simulation of pile driving is presented as an application to evaluate the efficacy of the proposed algorithm.

Successful implementation of hypoplastic sand model provides a framework for implementing an anisotropic visco-hypoplastic model of clay for more accurate simulation of soil structure for future works. Further, the sand can be modelled to be fully saturated, closely mimicking the real conditions of offshore pile installation. For future works, a rigid contact formulation may be developed and implemented for the interface element instead of the penalty contact formulation, eliminating the need for discretising the pile with material points, which would lead to savings in computational time.

Contents

List of Figures

List of Tables

Chapter 1

Introduction

1.1 Overview

Numerical simulation of physical processes have become an integral part in the field of science and engineering. History of finite element method, the primary tool used even today can be traced back to the 1940s when aircraft engineers were dealing with the invention of jet engine and needed a framework to analyse the airframe structures at large loads associated with high speeds. Without the benefit of modern computers, the engineers developed matrix methods of force analysis known as *flexibility method*, in which the displacements are known beforehand and unknowns are the forces. Finite element method, in its most used form corresponds to the *displacement method*, in which the unknown quantities are system displacements in response to applied force systems. During the following decades of 1960s and 1970s, finite element method was extended to applications including plate and shell bending, pressure vessels, general three-dimensional problems in elastic structural analysis, fluid flow and heat transfer applications. Further extensions to the finite element method to include the effects of large deflections and dynamic analysis also occurred around the same period. For applications in geo-mechanical simulation, fluid-structure interaction and in general, problems involving large deformations, the performance of FEM was not satisfactory. A need to formulate a new method to effectively simulate large deformation hence emerged.

As an improvement to the mesh-based method, meshless Lagrangian methods have been developed in which the continuum is described by a set of points as opposed to a FE grid. Each point represents a subregion of the deforming solid. Meshless methods circumvent the problem of mesh distortion, but perform poorly with regard to accurate application of boundary conditions and numerical integration. It might also not properly represent the considered continuum. If the density of point sets reduces during the deformation, non-physical gaps might occur within the discretised body, and numerical integration would either become inaccurate or fail altogether in that region. A well know method belonging to this class is *Smoothed Particle Hydrodynamics* (SPH).
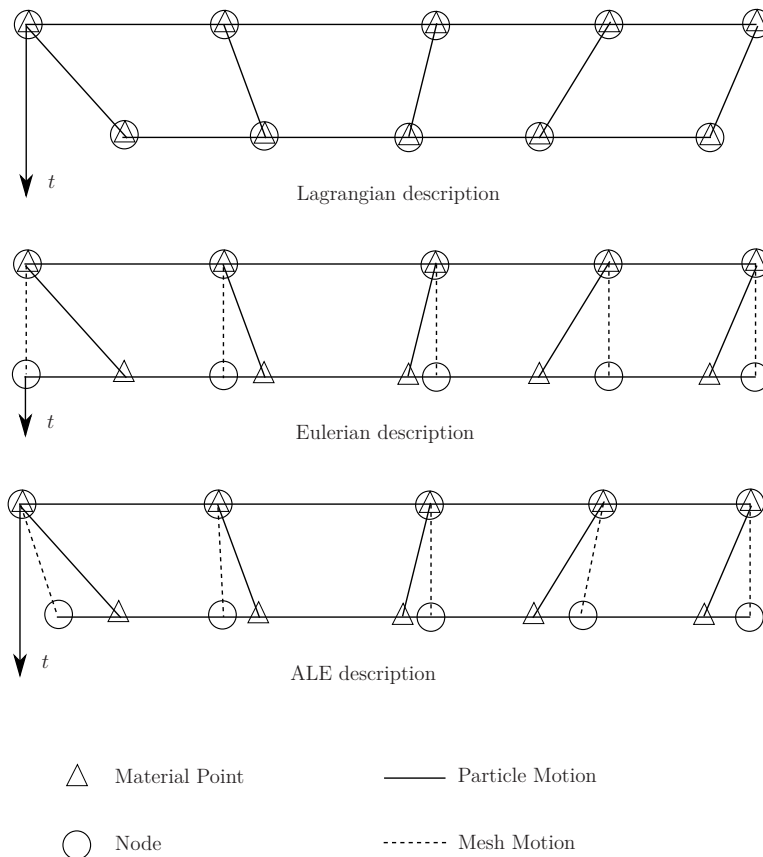
Figure 1.1: One-dimensional example of Lagrangian, Eulerian and ALE particle and mesh
        motion[19]

In Eulerian methods, the region of space that the continuum is moving through is discretised
instead of the continuum itself being subdivided into finite elements. An example of such a
method being the *Finite Volume Method*. It is possible to assess at a certain point of time
the velocity change that the particle experiences when passing by a grid node, or the amount
of material that crosses the element boundary. It is however not possible to determine from
such computations the location of the particle, or the velocity it has at a certain time.
Lagrangian method, however, allows tracing of the state variable of a certain particle as
the discretisaton of the state variable and the continuum are tied together. Usually with
solids, the equilibrium conditions are formulated with respect to the material and not to
the region surrounding it. Lagrangian methods are therefore more suitable to applications
in geotechnical problems as opposed to Eulerian methods.

In *Arbitrary Lagrangian-Eulerian* (ALE) methods, equilibrium conditions are solved on
the basis of a deforming mesh. The displacements do not necessarily coincide with the
movement of the particles during the computation. If mesh distortion becomes too large,
nodes uncouple from the particles that they follow. Particles of the continuum along with
its state variables move relative to the nodes of the mesh corresponding to the Eulerian
method. *Material Point Method* (MPM) is one such implementation of the ALE method.

MPM makes use of not only FE mesh as the background computational grid, but also a cloud of points, called material points which move through the computational grid which represent the continuum. The movement of material points represents deformation of the continuum. These material points carry the properties, state variables as well as the external loads. The background computational grid is used to determine the incremental displacements and strains. Information however, is not stored permanently in the computational grid. The mesh can then be reset, moved or changed arbitrarily. The three approaches are depicted in Figure 1.1. In this freedom with moving the computational node within the ALE description allows arbitrarily large deformation and helps avoid mesh entanglement.

In this work, CPDI, an enhanced version of classical MPM algorithm is used along with an improved contact algorithm involving penalty method, and has been used to simulate a pile installation problem. The constitutive model for hypoplastic sand has been employed to simulate the soil structure.

1.2 Scope of Work

Literature Study

A preliminary review on the existing numerical methods is made to understand the behaviour of each method under large deformation. This is carried out in order to understand the importance and position of Material Point Method in simulating continuum which undergo extreme deformation.

Development

1. A 2D finite element program with four gauss points is developed on the work of Al-Kafaji [1].

2. The hypoplastic constitutive model for sand is validated using this finite element program.

An extension of the finite element formulation to material point method (MPM) is studied and the MPM code developed by Dr.-Ing. F. Hamad is used for the treatment of large deformation problems

1. As opposed to the classical frictional contact method of MPM, a penalty contact method is applied between interacting surfaces to improve the accuracy of contact.

2. A simulation of a pile penetrating a soil structure is then simulated and compared with frictional MPM contact algorithm to highlight the differences.

Implementation

1. All the algorithms are implemented in programming language FORTRAN. The programs are compiled in Visual Studio using Intel Fortran Compiler.

2. Pre- and Post-Processing for the simulations carried out in the work is done in GiD 10.0.8.

Validation

The examples in this work have been validated using a commercial FE Tools - Plaxis 2D, for the validation of hypoplastic sand model, and ABAQUS, for the validation of results obtained from the MPM code, and also with other published literature.

1.3 Layout of the Thesis

The Thesis consists of 5 Chapters and it's arrangement follows the sequential order in which the work has been done. In addition, an Appendix is provided to understand the fundamental concepts of continuum mechanics.

Chapter 2 provides a brief history into the development of Material Point Method and the improvements that have been made to it. It provides the theoretical framework of CPDI, a improved version of MPM on which the simulations have been carried out on. It also provides an overview of the contact algorithm, the theoretical framework of the improved contact algorithm involving penalty contact that is used in applications presented in the subsequent chapters of the thesis.

Chapter 3 provides the theoretical framework of the hypoplastic sand model used in the simulations. Subsequently, the model's extension to small strain is also presented. Verification of the model is described with relevant validating examples.

In **Chapter 4**, a simulation of a pile penetrating into the soil is presented. The parameters of the sand model that has been used in the simulation as well as the boundary conditions and applied external forces are presented in the section. Finally, the result of the simulation is presented and is compared with results obtained from commercial FE package, ABAQUS.

The Thesis concludes with **Chapter 5** wherein the work is summarised and an outlook on the possible further works is discussed.

In addition, **Appendix A** provides a brief overview of continuum mechanics and provides an overview of notations used in this Thesis.

Chapter 2

Material Point Method - Overview

2.1 Introduction

For complex problems in continuum mechanics, it is not always possible to obtain a closed-form solution. The restrictions arise due to its geometry, loads or boundary conditions. It became essential to develop alternate procedures that yield an approximate solution. Several numerical methods have been developed over the last decade, but none were as popular and widely used as the finite element method. In computational mechanics, the *Finite Element Method* (FEM) is a numerical technique that approximates the solution of boundary value problem. Finite Element method has been successfully applied to a wide range of problems in both solid and fluid mechanics with very good results. For three-dimensional problems however, FE meshes can often be too complex and time consuming to solve. Further, large deformation leads to mesh distortion and might require re-meshing. These difficulties led to the development of alternate discretisation strategies which avoids mesh distortion by discretising at point and by not maintaining a body-fixed mesh.

A number of meshless methods have been developed. The main differences between these methods depends on facts whether or not a temporary mesh is included in the solution procedure, whether discretisation procedure begins with the weak form or the differential equation, and in the construction and support of the point weighting functions. One of the methods that is developed is the Partition of Unity method. This method uses a variational form to specialise the discrete approximation in regions of the problem domain using a standard Galerkin discretisation scheme. This is in contrast to the development from a variational form by using a Petrov–Galerkin discretisation scheme, for methods such as Adaptive Characteristic Petrov–Galerkin Finite Element, and Meshless Local Petrov–Galerkin methods. Later, mesh-based particle method are developed, which consists of a pre-defined background mesh and particles representing the continuum which move within this background mesh. A typical representation of a MPM discretisation is presented in Figure 2.1.
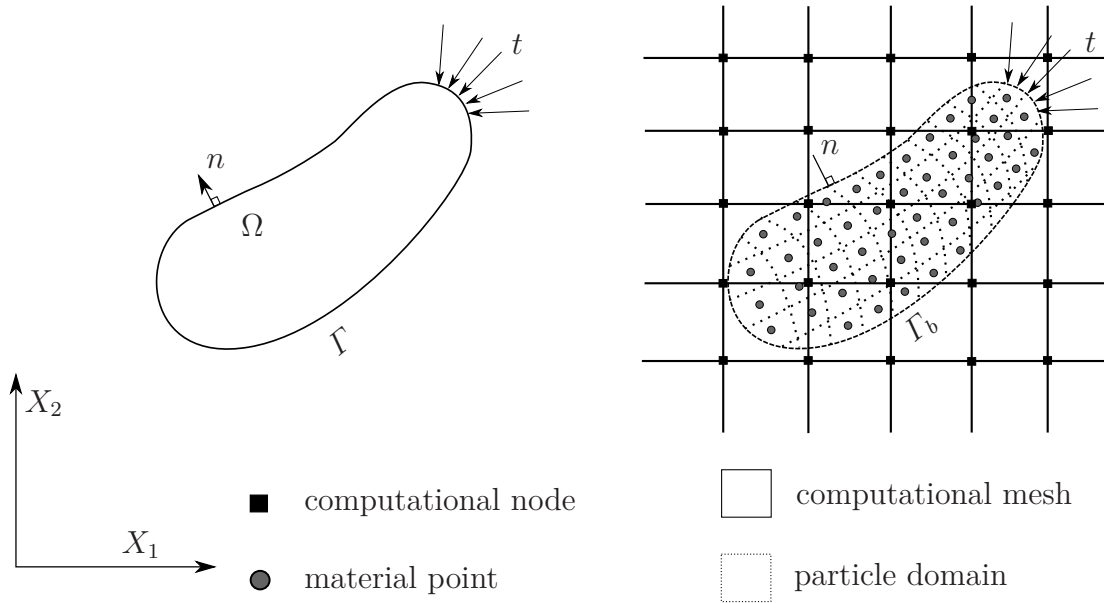
Figure 2.1: Representation of MPM discretisation

2.2 Mesh-free Methods

In meshless methods, the nodal connectivity is adjusted continuously as the continuum deforms. This avoids the problem of mesh-distortion. The approximations in the meshless method can be based on moving least-squares method, kernels or partition of unity methods. The earliest implementation of meshless method is presented by Lucy [40], and is called *Smoothed Particle Hydrodynamics* (SPH). SPH is a particle method in which the closed form of the partial differential equation is approximated using collocation methods. SPH method does not require a pre-defined mesh to calculate the spatial derivatives, a clear distinction from the material point method.

Another relatively younger mesh-free method is the *Element-free Galerkin* Method (EFG) [9]. In this method, the trial functions for the weak form are constructed using the moving least-squares interpolation. Oñate et al. [51] has presented the *Particle Finite Element Method* (PFEM) in which the nodal points represent the particles and computational mesh is constructed by connecting these points. The mesh is then used to solve the governing equations in a Lagrangian fashion.

Meshless methods are suited to problems involving large deformation, but still require considerable improvement in computational efficiency. It is shown that the computational cost of (EFG) method is much higher than that of conventional FEM. A few other mesh-free methods that are popular include *Extended Finite Element Method* (XFEM) and *Smoothed Finite Element Method* (SFEM).

2.3 Mesh-based Particle Methods

In mesh-based particle methods, certain features of both the meshless and the mesh-based methods are exploited to simulate large deformation problems effectively, which otherwise would be impossible in either of the methods separately. Unlike the mesh-free methods where there is a strict absence of background mesh, in mesh-based particle methods, there is a pre-defined background computational mesh where the material points represent the continuum and move within the background mesh as it deforms.

2.3.1 Particle-in-cell Method

The first *Particle-In-Cell* (PIC) simulations have been carried out in the late 1950s by Buneman [14] and Dawson [18] where the motion and interaction of upto 1000 particles have been simulated. Although the original objective was to simulate problems in two- and three- dimensions, the early developments of PIC has been limited to one-dimension [24].

With time, limitations of PIC became evident. It was noisy, has more numerical viscosity [12] and suffers from energy dissipation [1]. The reason for this dissipation is attributed to the fact that Harlow's original formulation was partially Lagrangian, in the sense that only mass and position were assigned to each particle. Other physical properties such as velocity, momentum and energy are temporarily mapped to the particles in order to convect information between cells at the end of each time step. The properties assigned to particles are weighted by the mass of each particle. If a particle moves from one cell to another, the energy and momentum associated with it are subtracted from the old cell and added to the new cell. They are not stored permanently within the particle, which makes it more of an Eulerian method. In spite of such drawbacks, PIC was successful in simulating problems involving large distortion [25]. Nishiguchi and Yabe [50] develops a more accurate scheme for the convection between particles and grid points. Although they use the *partially Lagrangian* representation of particles as in the original PIC, they improved the accuracy of momentum advection and energy to a second order accuracy in space. Considerable improvements have been later made to modify the *partially Lagrangian* representation of particles to a *fully Lagrangian* representation in which the physical quantities such as momentum and energy are assigned to the particles. The grid is then used to solve for the solution of governing equations. As a consequence of using a *fully Lagrangian* approach, reduced numerical diffusion is achieved. This improvement, however, meant that additional storage is required compared to the *partially Lagrangian* formulation.

2.3.2 Fluid-implicit particle method

Brackbill and Ruppel [13] uses the *fully Lagrangian* PIC as a basis to extend the applicability of the method by using adaptively zoned mesh. It is then developed to a method called *Fluid-Implicit Particle* method (FLIP), which is a PIC formulation in which the particles carry the physical properties like mass, momentum and constitutive properties of the continuum. As a direct consequence of using an adaptive mesh, simulation of complex geometries with better accuracy is achieved. Furthermore, the computational cycle of PIC to Lagrangian and Eulerian phase is clearly separated. This separation allows the use of existing finite difference algorithms to solve the discrete equations in the Lagrangian phase, as particles do not play a permanent role in this phase.

FLIP is extended to problems involving Fluid-Structure interactions by Sulsky and Brackbill [63]. This method is naturally capable of handling non-slip contact between different bodies without any special algorithm [64]. This is due to the fact in PIC, particle velocities are single valued in mapping and re-mapping between grid points and the particles.

Burgess et al. [15] demonstrates that mapping of velocities from particles to nodes can be made conservative on the basis of mass-weighted least square procedure. This procedure requires inversion of mass-matrix to compute velocities from momentum. It has been already shown that conservation of kinetic energy is fully achieved if consistent mass-matrix is used, inversion of the matrix however, is computationally expensive. Alternatively, a lumped-mass matrix is used where the diagonal entries correspond to the row sum of the consistent-mass matrix. Although using a lumped-mass matrix has both computational and storage advantages, it introduces numerical dissipation in the kinetic energy.

2.3.3 Coupled Eulerian Lagrangian Method

In order to validate the results obtained from the MPM code, a commercial FE package ABAQUS is used. In order to simulate the pile installation in ABAQUS, a problem with large deformations, the *Coupled Eulerian-Lagrangian* (CEL) method is employed. With this method, the drawback of the FE method, which originates from its reliance on a Lagrangian mesh is overcome. The CEL method is based on coupling between the Lagrangian body, which most commonly is the solid material, and the Eulerian body for the fluid behaviour material. Explicit coupling is obtained by applying pressure boundary condition on the Lagrangian body whereas velocity boundary condition is prescribed on the Eulerian discretisation of the fluid, as demonstrated in Figure 2.2. This method is chosen for ABAQUS simulation as its applicability in geomechanical applications has been proven for Lagrangian object being pushed into an Eulerian soil [46, 53].
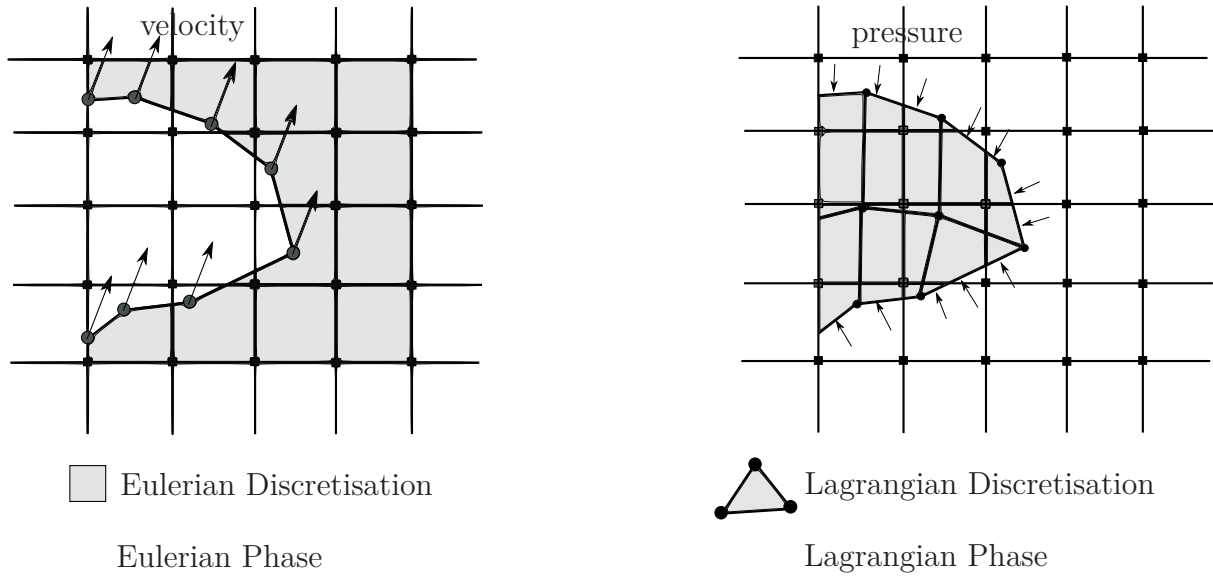
Figure 2.2: Explicit coupling in Coupled Eulerian-Lagrangian (CEL) Method

2.4 Material Point Method

Material point method (MPM) is a sophisticated technique suitable for simulating large deformation. In MPM, continuum is represented by *Lagrangian points*, known as *Material Points*. Large deformations are modelled by particles moving through the fixed Eulerian mesh. In this formulation, the particles carry all the physical properties of the continuum like momentum, mass, material parameters, stresses, strains and external loads. The fixed Eulerian mesh and its Gauss points do not carry any permanent information during the solution. At the beginning of each solution step, information is mapped from the particles to computational grid. Incremental solution is determined in the grid in a Lagrangian fashion. At the end of solution step, the information is mapped back to the particles. A representation of a MPM computational step is presented in Figure 2.3.

2.4.1 History of development of MPM

FLIP method is extended for use in solid-mechanics by Sulsky et al. [64]. The weak formulation of the discrete equations is formulated such that they are consistent with the traditional finite element method. Furthermore, constitutive equations are applied to each particle, thereby avoiding interpolation of history dependent variables. Each particle is tracked separately during the computation process. Due to MPM's formulation of applying constitutive equation separately to each particle, continuum with different material parameters or constitutive equations are automatically treated, which is a clear advantage over Eulerian FEM. Numerical examples with large rigid-body rotations show that the energy dissipation which tends to occur in Eulerian approach does not occur in the proposed ap-

initial position   incremental deformation   end of time step
deformation of particles
reset of mesh
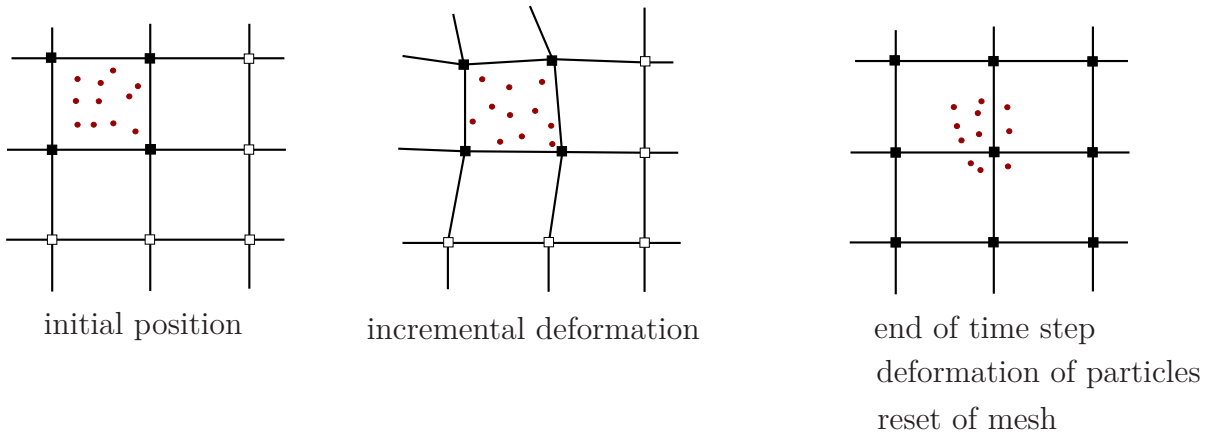
Figure 2.3: Computational step in MPM

proach. This method is implemented in impact of objects in plane-strain configuration with elastic and strain-hardening plastic material behaviour [59]. To incorporate constitutive laws expressed in terms of Jaumann stress rate, PIC is extended in the work of Sulsky and Schreyer [60]. An axi-symmetric formulation of PIC is formulated and named as Material Point Method (MPM) where examples of elastic vibration of sphere and taylor-bar impact is presented [61].

Więckowski et al. [67] applies MPM to simulate flow of granular material during the process of discharging a silo. The phenomenon of friction is taken into account and frictional contact algorithm and solution procedure for contact problems is presented in the framework of MPM. A framework for calculating the critical time step is suggested and derived from stability criterion. It is observed that among the mesh size and the wave speed, the critical time step is significantly affected by the number and position of particles in the elements. It is also observed that in general, MPM demands a smaller time step size than FEM. Bardenhagen and Brackbill [4] investigates stress localisation in granular materials and discusses its application to plastic-bonded explosives. Observations for quasi-static and dynamic loading is also discussed. Coetzee [16] discusses the application of MPM to model the flow of granular material in front of flat bulldozer blades and into dragline type buckets. The formulation is based on Cosserat continuum, and MPM results is compared with experimental measurements, along with results obtained from discrete element method.

Guilkey et al. [21] formulates a quasi-static MPM approach to simulate slow rate of loading. The formulation is applied to the modelling of multicellular constructs. An implicit integration scheme is used to integrate the equilibrium equation. As opposed to traditional MPM, resetting of mesh after each time step is avoided. The reason is to mitigate error associated with particle crossing between elements, which is know to cause errors in quasi-static analysis due to absence of inertia forces.

Bardenhagen and Kober [5] generalises the MPM solution procedure with a smoother spline interpolation function with a larger influence region and a continuous first order gradient

called *Generalised Interpolation Material Point* method GIMP. The main motivation behind the development of GIMP is to eliminate the numerical noise associated with MPM when particles cross element boundary. Also, when the boundaries of particle domains become misaligned with the grids under rotation, the computation of interpolation functions becomes very complex. To avoid this problem, Sadeghirad et al. [55] proposes a new method, *Convected Particle Domain Interpolation* method (CPDI) using alternate grid basis functions. Instead of considering rectangular particle domains, they are considered as parallelograms.

2.4.2 Implicit integration in MPM

In dynamic MPM, solution is usually advanced using explicit time integration scheme. However, in quasi-static problems, where the flow of material is slower than the wave speed propagating through the material, computations is time consuming. Employing an implicit integration scheme reduces computation time considerably. Cummins and Brackbill [17] proposes an implicit formulation and applies it to quasi-static simulation of granular materials. An inexact, matrix-free, Newton-Krylov technique is used to solve the fully implicit, non-linear equations of motion for granular flows with inter-granular contact. This technique is adopted to reduce computation time by eliminating the construction of tangent stiffness matrix. A similar approach with different time discretisation is implemented by Sulsky and Kaul [58]. It is shown that implicit solver generates solution whose accuracy is compromised in problems where the time step size is large, as there is some energy dissipation when applied to problems of high frequency content. In the work of Love and Sulsky [39], it is shown that an implicit formulation of MPM is unconditionally stable. By constructing a consistent mass matrix together with the implicit scheme, the algorithm's complexity is significantly increased. In addition to implicit algorithm of dynamic MPM, there also exists quasi-static formulation with implicit solvers [11].

2.5 Numerical Formulations of Dynamic Material Point Method

Similar to formulation in FEM [32], numerical formulation in MPM begins from the weak form of momentum balance equation. Momentum balance equation describes the equation of motion of a body [32] and is given by

$$\rho \, \dot{\boldsymbol{v}} = div(\boldsymbol{\sigma}) + \rho \, \boldsymbol{g} \, , \tag{2.1}$$

where, ρ is the density, $\boldsymbol{g}$ is the gravitational field, $\boldsymbol{u}$ is the displacement field, $\boldsymbol{v}$ is the velocity field, and $\boldsymbol{\sigma}$ is the Cauchy stress. Rewriting Equation 2.1 in indices notation, we

get

$$\rho \, \frac{dv_i}{dt} = \frac{\partial \sigma_{ij}}{\partial x_j} + \rho \, g_i \, . \tag{2.2}$$

The equations presented is referred to as the strong form. A weak form is derived to be used in the discretised form. This is done by multiplying the strong form with a test function, $\delta \boldsymbol{u}$ and integrating over the entire domain, Ω. The weak form of Equation 2.2 is represented as

$$\int_\Omega \delta u_i \, \rho \, \frac{dv_i}{dt} \, d\Omega = \int_\Omega \delta u_i \, \frac{\partial \sigma_{ij}}{\partial x_j} \, d\Omega + \int_\Omega \delta u_i \, \rho \, g_i \, d\Omega \, , \tag{2.3}$$

with,

$$\delta u_i = 0 \, on \, d\Omega \, . \tag{2.4}$$

By applying integration-by-parts rule on the first part of Equation 2.3, and substituting it back, we get

$$\int_\Omega \delta u_i \, \rho \, \frac{dv_i}{dt} \, d\Omega = \int_\Omega \frac{\partial}{\partial x_j} \left(\delta u_i \sigma_{ij} \right) d\Omega - \int_\Omega \frac{\partial(\delta u_i)}{\partial x_j} \, \sigma_{ij} \, d\Omega + \int_\Omega \delta u_i \, \rho \, g_i \, d\Omega \, . \tag{2.5}$$

By applying Gauss's theorem to the first term of Equation 2.5, we get

$$\int_\Omega \frac{\partial}{\partial x_j} \left(\delta u_i \, \sigma_{ij} \right) d\Omega = \int_\Gamma \delta u_i \, \sigma_{ij} \, n_j \, d\Gamma \, , \tag{2.6}$$

with, Γ the boundary of the domain Ω. Substituting Equation 2.6 in Equation 2.5 yields the weak form of the momentum balance equation

$$\int_\Omega \delta v_i \, \rho \, \frac{du_i}{dt} \, d\Omega = \int_\Omega \delta u_i \, \rho \, g_i \, d\Omega - \int_\Omega \frac{\partial(\delta u_i)}{\partial x_j} \, \sigma_{ij} \, d\Omega + \int_\Gamma \delta u_i \, t_i \, d\Gamma \, , \tag{2.7}$$

where, traction $t_i = \sigma_{ij} \, n_j$ is obtained using Cauchy's lemma.

The values of a variable inside an element is based on the nodal values and the corresponding shape function denoted by N_i. In MPM, a body is represented by a group of particles. An additional step is required to interpolate the fields to and from the particles. Integrals here are approximated as a sum over the particles and represented as

$$\int_\Omega \rho(*) \, d\Omega \approx \sum_p \int_{V_p} \rho(*) \, dV_p \approx \sum_p \int_p (*) \, m_p \approx \sum_p (*) \, m_p \, , \tag{2.8}$$

where, m_p is the mass associated with the material point p, and V_p is the particle volume. Using these definitions, the discretised momentum equation takes the form

$$\boldsymbol{M} \, \ddot{\boldsymbol{a}} = \boldsymbol{F}^{ext} - \boldsymbol{F}^{int} \, , \tag{2.9}$$

where, $\boldsymbol{M}$ is the consistent mass matrix, $\ddot{\boldsymbol{a}}$ the acceleration vector, and $\boldsymbol{F}^{ext}$ and $\boldsymbol{F}^{int}$ are external and internal force vectors, respectively. Using a lumped-mass matrix significantly simplifies calculation due to its diagonal nature, despite introducing a slight amount of

numerical dissipation, it is preferred over consistent mass matrix. In the element level, it is represented as

$$m_i = \sum_{p=1}^{n_p} m_p \ N_i(\boldsymbol{x}_p) \ , \tag{2.10}$$

where, n_p is the number of material point, and $\boldsymbol{x}_p$ indicates the location where shape function N_i is evaluated. Referring to Equation 2.9, the external force vector is given by

$$\boldsymbol{F}^{ext} = \sum_{p=1}^{n_p} m_p \ \boldsymbol{N}^T(\boldsymbol{x}_p) \ \boldsymbol{g} + \int_{\Gamma} \boldsymbol{N}^T \ \boldsymbol{t} \ d\Gamma \ , \tag{2.11}$$

and, the internal force vector is given by

$$\boldsymbol{F}^{int} = \sum_{p=1}^{n_p} V_p \ \boldsymbol{B}^T(\boldsymbol{x}_p) \ \boldsymbol{\sigma}_p \ , \tag{2.12}$$

where, $\boldsymbol{B} = \boldsymbol{L}\boldsymbol{N}$ with $\boldsymbol{L}$ being the linear differential operator, and $\boldsymbol{\sigma}_p$ is a vector containing the stress components at material point p.

The equations presented above describe the procedure for solving the unknown quantities at the computational node. Care must be taken when including forces with surface traction. One of the approach followed to accommodate tractions is to assign the corresponding forces to the nearest material point [1]. After computing the forces and building the mass-matrix, the particle's state and its position is updated at the end of computational time step by resetting the computational mesh.

2.5.1 Time Integration

Given a diagonal mass-matrix, integration of the system of equation over time becomes trivial. Acceleration vector is given by

$$\ddot{\boldsymbol{a}}^n = [\boldsymbol{M}_l^n]^{-1} \left(\boldsymbol{F}^{ext} - \boldsymbol{F}^{int} \right)^n \ , \tag{2.13}$$

where a forward-Euler time integration scheme is used to update the nodal velocity from the nodal accelerations. In practice, however, a modified algorithm proposed by Sulsky et al. [62] is used. The nodal velocities of the particle is updated using the equation

$$\dot{\boldsymbol{a}}_p^{n+1} = \dot{\boldsymbol{a}}_p^n + \sum_{i=1}^{ndof} \Delta t \ N_i(\boldsymbol{x}_p) \ \ddot{\boldsymbol{a}}_i^n \ , \tag{2.14}$$

where, $ndof$ represents the number of grid degrees of freedom, $\dot{\boldsymbol{a}}_p^n$ and $\dot{\boldsymbol{a}}_p^{n+1}$ are the velocities of particle p at the beginning and end of time step Δt, respectively. Nodal velocities are then mapped from the particles to the nodes, being aware of the restriction that momentum must be conserved. It is given by

$$\boldsymbol{M}_l^n \dot{\boldsymbol{a}}^{n+1} = \sum_{p=1}^{n_p} m_p \ \boldsymbol{N}^T(\boldsymbol{x}_p) \ \dot{\boldsymbol{a}}_p^{n+1} \ , \tag{2.15}$$

where, $\dot{\boldsymbol{a}}^{n+1}$ is the updated nodal velocity. It is then used to obtain incremental nodal displacement via the relation

$$\Delta \boldsymbol{a} = \Delta t \ \dot{\boldsymbol{a}}^{n+1} \ . \tag{2.16}$$

Position of the particle is updated via the relation

$$\boldsymbol{x}_p n + 1 = \boldsymbol{x}_p^n + \boldsymbol{N}(\boldsymbol{x}_p) \ \Delta \boldsymbol{a} \ , \tag{2.17}$$

where, $\boldsymbol{x}_p^n$ and $\boldsymbol{x}_p^{n+1}$ are positions of particle at time t^n and t^{n+1}, respectively. Since the position of particle is updated using a single-valued continuous velocity field, interpenetration of particles is avoided. This also allows an automatic no-slip contact between the bodies without the need for a separate contact algorithm. After obtaining the updated nodal velocities, strain increment $\Delta \boldsymbol{\epsilon}_p$ of material point p is calculated using the relation

$$\boldsymbol{\epsilon}_p = \boldsymbol{B}(\boldsymbol{x}_p) \ \Delta \boldsymbol{a}_e \ , \tag{2.18}$$

where, $\Delta \boldsymbol{a}_e$ is vector of incremental nodal displacements of element e to which the material point belongs. Given the strain increment, stress increment $\Delta \boldsymbol{\sigma}_p$ is updated at each material point using the constitutive law unique to that material point. Total stresses are updated via the relation

$$\boldsymbol{\sigma}_p^{n+1} = \boldsymbol{\sigma}_p^n + \Delta \boldsymbol{\sigma}_p \ , \tag{2.19}$$

where, $\boldsymbol{\sigma}_p^n$ and $\boldsymbol{\sigma}_p^{n+1}$ are global stresses at time t^n and t^{n+1}, respectively.

2.5.2 Numerical formulation of CPDI

Sadeghirad et al. [55] proposes the *Convected Particle Domain Interpolation* method (CPDI) by using alternative grid basis functions. Instead of rectangular grid basis functions, the particles are considered as parallelograms and thus large deformations of a single phase material can be well simulated. CPDI permits the initial particle domain to be a parallelogram and at the end of the time step, the parallelogram is updated using the deformation gradient $\boldsymbol{F}_p^n$. Since early MPM versions assumed a collocated distribution for the material properties across the particle domains, it causes numerical instability when particles crosses element boundaries, termed as cell-crossing error. Updating the particle domain in CPDI reduces the cell-crossing error as well as the extension instability, when the influence of supporting domains no longer overlap with other particles. Linking the influence of particles with its deformations can cause numerical difficulties in the integration of constitutive equation when the particle is heavily distorted. To address this problem, Homel et al. [29] introduces a geometrical resizing procedure to limit the particle domain size within a fixed circle, whereas the deformation gradients contributing to the material model are kept intact. Numerical freezing of a particle influence is applied to accommodate the material separation and improve the accuracy of CPDI near the centre line of an axi-symmetric problem [45]. Sadeghirad et al. [56] extends the CPDI formulation where the level of interpolation is extended and the particles evolve to quadrilaterals from parallelograms and is termed as

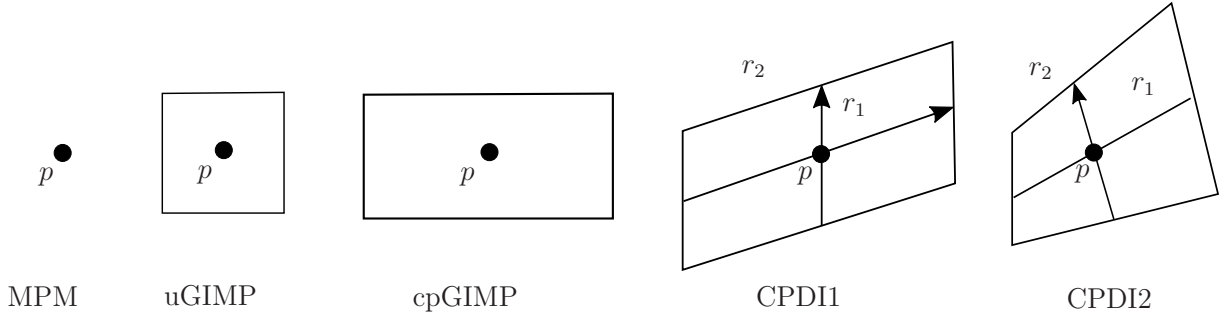MPM   uGIMP   cpGIMP   CPDI1   CPDI2

Figure 2.4: Evolution of domains to represent the material point in MPM[22]

CPDI2. CPDI method has been implemented in this work and further formulations would only deal with CPDI. The enhancement of particle domains is represented in Figure 2.4.

Recalling the discretised momentum balance equation associated with node i

$$M_i \boldsymbol{a}_i = \boldsymbol{F}^{ext} - \boldsymbol{F}^{int} \ , \tag{2.20}$$

where, $\boldsymbol{a}_i$ is the nodal acceleration vector associated with node i. The lumped mass M_i, and the nodal force vectors are represented as

$$M_i = \sum_p \phi_{ip} \ m_p \ , \tag{2.21}$$

$$\boldsymbol{F}^{ext} = \sum_p \phi_{ip} \ \boldsymbol{g} \ m_p \ + \ \int_{\Gamma_p} \boldsymbol{\tau} \ \phi_i(\boldsymbol{x}) \ d\Gamma \ , \tag{2.22}$$

$$\boldsymbol{F}^{int} = \sum_p \nabla \phi_{ip} \ \boldsymbol{\sigma}_p \ V_p \ , \tag{2.23}$$

where, ϕ_{ip} is a mapping function and the subscript denotes the coupling between grid quantities i and particle-based quantities p. m_p, V_p and $\boldsymbol{\sigma}_p$ are the mass, volume and stress tensor corresponding to the particle p, respectively. In CPDI, the alternative basis functions are constructed to be an interpolation of standard basis functions at the four corners of each particle domains [55] and represented as

$$\phi_{ip} \cong \frac{1}{4} \left[S_i(\boldsymbol{x}_1^p) + S_i(\boldsymbol{x}_2^p) + S_i(\boldsymbol{x}_3^p) + S_i(\boldsymbol{x}_4^p) \right] \ , \tag{2.24}$$

where, $S_i(\boldsymbol{x}_j^p)$ is the grid basis function of the corner $j \in [1, 2, 3, 4]$ of the parallelogram domain of the particle p. The gradient of interpolation function is obtained accordingly as

$$\nabla \phi_{ip} = \frac{1}{2V_p} \left\{ \left[S_i(\boldsymbol{x}_1^p) - S_i(\boldsymbol{x}_2^p) \right] \begin{bmatrix} r_{1z}^n - r_{2z}^n \\ r_{2x}^n - r_{1x}^n \end{bmatrix} + \left[S_i(\boldsymbol{x}_2^p) - S_i(\boldsymbol{x}_4^p) \right] \begin{bmatrix} r_{1z}^n + r_{2z}^n \\ -r_{1x}^n - r_{2x}^n \end{bmatrix} \right\} \ , \tag{2.25}$$

where, $\boldsymbol{r}_1$ and $\boldsymbol{r}_2$ are the vectors defining the parallelogram domain, as shown in Figure 2.4. These vectors are updated according to the relation

$$\boldsymbol{r}_1^{n+1} = \boldsymbol{F}_p^{n+1} \cdot \boldsymbol{r}_1^0 \ , \tag{2.26}$$

$$r_2^{n+1} = F_p^{n+1} \cdot r_2^0 \,, \tag{2.27}$$

where, $\boldsymbol{F}$ denotes the deformation gradient of material point p, and the superscripts 0 and $n+1$ denote the initial and updated vectors, respectively. Deformation gradient is updated continuously through the relation

$$F_p^{n+1} = \left(\boldsymbol{I} + \nabla \boldsymbol{v}_p^{n+1} \, \Delta t \right) F_p^n \,, \tag{2.28}$$

where, $\boldsymbol{I}$ is the second-order identity tensor, and Δt is the time step increment. The velocity gradient is obtained by interpolation of the nodal velocities and is given by the relation

$$\nabla \boldsymbol{v}_p^{n+1} = \sum_p \nabla \phi_{ip} \, \boldsymbol{v}_i^{n+1} \,. \tag{2.29}$$

The gradient $\nabla \phi_{ip}$ is evaluated using the relation

$$\nabla \phi_{ip} = \frac{1}{V_p} \int_\Omega \nabla \phi_i dV \,, \tag{2.30}$$

and the nodal velocity $\boldsymbol{v}_i^{n+1}$, at the end of the time step is obtained using the procedure proposed by Sulsky et al. [62]. This is represented as

$$v_i^{n+1} = \frac{\sum_p \phi_{ip} m_p \boldsymbol{v}_p}{m_i} + \boldsymbol{a}_i \Delta t \,, \tag{2.31}$$

where, $\boldsymbol{a}_i$ is obtained from Equation 2.13. The particle velocity is updated through direct mapping of the grid information and the position of material points is advanced using the nodal velocity achieved by applying principle of momentum conservation according to the least squares concept. The updates are expressed as

$$v_p^{n+1} = v_p^n + \sum_i \phi_{ip} \, \boldsymbol{a}_i \, dt \,, \tag{2.32}$$

$$x_p^{n+1} = x_p^n + \sum_i \phi_{ip} \, \boldsymbol{v}_i \, dt \,. \tag{2.33}$$

2.6 Contact Formulation in MPM

This section presents a brief history of modelling contact in MPM and the numerical formulation of penalty function method implemented in the contact algorithm.

2.6.1 History of contact formulations in MPM

Modelling frictional contact is a widely encountered problem in simulation science and has been effectively simulated by MPM. As MPM uses a single-valued mapping function between background grid nodes and particles, interpenetration of particles is avoided in standard MPM formulation. A no-slip contact constraint is also inherent in standard MPM. In the work of Sulsky et al. [62], where a steel sphere impacts an aluminium target, it is shown that due to inherent no-slip condition, a greater penetration resistance is developed. A simple contact algorithm is proposed by York [70] to allow the release of no-slip constraint in standard MPM. York [70] proposes that if the bodies come into contact with each other, standard MPM method is used to impose the impenetrability condition, and if the bodies move away from each other, they move in their own velocity fields to allow separation. Bardenhagen et al. [7] introduces the early contact algorithm to relax the interaction between objects, and also proposes a contact/friction/separation algorithm in multi-velocity fields. The impenetrability condition and the Coulomb friction are incorporated into the MPM algorithm when contact occurs. This approach is demonstrated using the sphere rolling on the inclined plane and the granular shear simulation [8]. Xiao-Fei et al. [69] proposes a three-dimensional multi-mesh contact algorithm, in which the contact force between the bodies is obtained from the normal nodal acceleration continuity requirement at the contact surface. This approach is used to simulate impact of Taylor bar and that of elastic and plastic spheres.

In the approaches described until now, contact is detected when material points of different bodies contribute to the same grid node of the background computational mesh. This leads to interaction being activated before the contact actually taking place. Furthermore, lack of smoothening function in detection procedure causes oscillation in contact stresses. Ma et al. [41] presents a new contact algorithm in MPM, named *Geo-contact* developed especially for geotechnical simulation, with a penalty contact function and a limited maximum shear stress. The penalty function improves the accuracy of the computation via reducing numerical oscillation in the quantitative contact forces by avoiding impact of the contacting materials. The limited maximum shear stress along the interface facilitates the simulation of different contact conditions in terms of geotechnical engineering. In order to avoid the non-physical behaviour that corresponds to the velocity field algorithm [6], an approach based on the combination of multi-mesh is suggested by Hu and Chen [30]. Simulation of contact between the teeth of Spur gears is simulated and also has been applied for numerous other applications [42].

Although MPM is more accurate and robust for problems involving severe distortion than FEM, it is less efficient that FEM for problems involving small deformation. This is because MPM demands more computational cost and storage as it saves both grid and particle data. It is therefore desirable to couple MPM and FEM to take advantage of both methods. For advanced versions of MPM like GIMP and CPDI, where the spatial size is assigned to the material points, the opening between bodies in contact become more pronounced [5, 55, 56]. This also leads to the requirement of a more precise definition of the contact surface, which can be ensured using a finite element formulation.

Attaway et al. [3] demonstrates the coupling between SPH and FEM through a master-slave algorithm, where the contact forces is imposed on the master surface and the slave particles to avoid penetration. Johnson and Stryk [31] extends the coupled particle method by converting damaged or failure elements into particles. In the work of Zhang et al. [71], the material domain is discretised by a mesh of finite elements, and a computational grid is predefined in the potential large deformation zone. The nodes covered by the grid are treated as MPM particles, and the remaining nodes are treated as FE nodes.In the coupled finite element-material point method [35], the FEM and MPM body are coupled using the local multi-mesh contact method. In the adaptive finite element-material point method [36], all bodies are initially discretised as finite elements, the distorted/failed elements are automatically converted to particles during the simulation. The converted particles are coupled with the remaining FEM nodes using the local multi-grid contact method.

2.6.2 Frictional contact algorithm

In the basic MPM formulation, a non-slip condition is automatically imposed between the objects coming into contact to prevent interpenetration. This condition adds extra resistance when the bodies are coming into contact. Furthermore, if the bodies move away after contact, due to the non-slip condition imposed, MPM algorithm glues the bodies together. This fact is illustrated in the work of Sulsky et al. [62] where an elastic sphere impacts an elastic-perfectly plastic material. The non-physical gluing of objects exists when they share a computational node. Refining the mesh neither solves the problem, nor does it smoothen it. An additional contact algorithm is therefore required to alleviate this problem.

As an improvement York [70] introduces a criterion to check whether the bodies are approaching each other, or are they moving apart. If the bodies are moving towards one another, the standard MPM method is used. The material points are moved in the usual 'centre-of-mass' velocity field which enforces the no-penetration condition. If the bodies are moving away from one another, they are allowed to move in their own velocity field, which allows separation to occur. As an advancement to the simple separation algorithm, Bardenhagen et al. [7] proposes an algorithm which allows sliding and rolling with friction. The traction due to momentum is added as an external force while solving the discretised
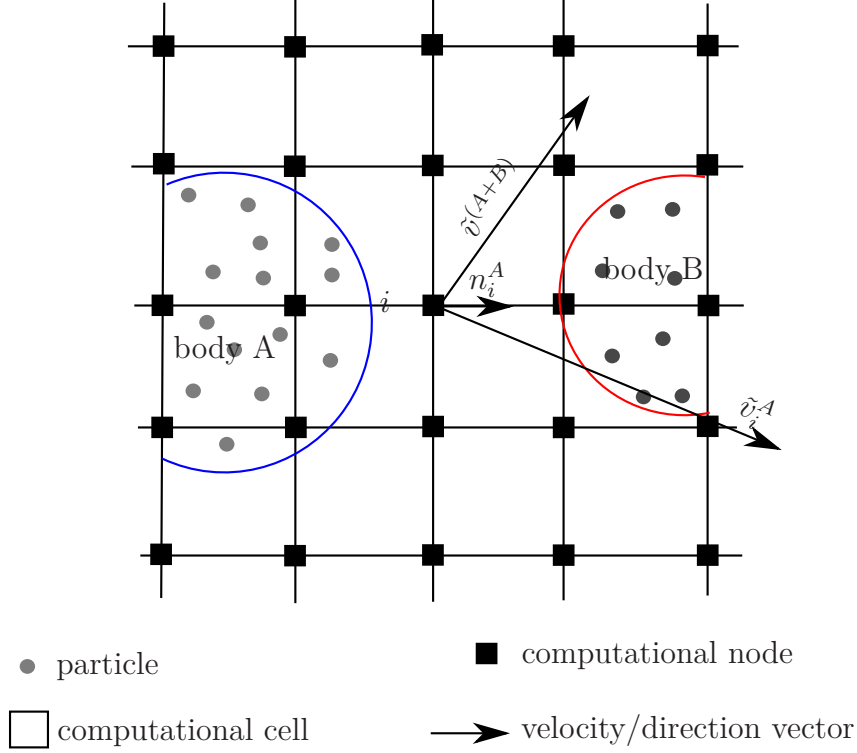
Figure 2.5: Correction procedure in frictional contact algorithm[22]

momentum equation, Equation 2.9. The solution of this equation is performed separately for each body in contact. An extra solution for the combination of the bodies is required. The equation of motion is thus solved as many times as the number of bodies in contact plus one. The MPM procedure is applied only when the following inequality is satisfied

$$(\tilde{\boldsymbol{v}}_i^{n+1,A} - \tilde{\boldsymbol{v}}_i^{n+1,(A+B)}) \cdot \boldsymbol{n}_i^{n,A} > 0, \tag{2.34}$$

where, $\boldsymbol{n}_i^{n,A}$ is the outward unit normal of body A at node i at the beginning of the time step. $\tilde{\boldsymbol{v}}_i^{n+1,A}$ and $\tilde{\boldsymbol{v}}_i^{n+1,(A+B)}$ are the velocities of body A and the combination of bodies A and B, respectively. The visual illustration of the relation is presented in Figure 2.5. If a difference in velocities between the individual entities and the combination of the entities is detected, the interpenetration of bodies is deterred applying the correction described by the relation

$$\tilde{\tilde{\boldsymbol{v}}}_i^{n+1,A} \cdot \boldsymbol{n}_i^{n,A} = \tilde{\boldsymbol{v}}_i^{n+1,(A+B)} \cdot \boldsymbol{n}_i^{n,A}, \tag{2.35}$$

with $\tilde{\tilde{\boldsymbol{v}}}_i^{n+1,A}$ being the modified velocity of the body A that is adjusted according to the normal component of the system solution. Equation 2.35 is rewritten involving Equation 2.34 in the form

$$\tilde{\tilde{\boldsymbol{v}}}_i^{n+1,A} = \tilde{\boldsymbol{v}}_i^{n+1,A} - \left[\left(\tilde{\boldsymbol{v}}_i^{n+1,A} - \tilde{\boldsymbol{v}}_i^{n+1,(A+B)} \right) \cdot \boldsymbol{n}_i^{n,A} \right] \boldsymbol{n}_i^{n,A}, \tag{2.36}$$

where the correction term is understood as an external force applied at the interface node such that

$$\boldsymbol{f}_{i,norm}^{n+1,A} = -\frac{m_i^{n,A}}{\Delta t} \left[\left(\tilde{\boldsymbol{v}}_i^{n+1,A} - \tilde{\boldsymbol{v}}_i^{n+1,(A+B)} \right) \cdot \boldsymbol{n}_i^{n,A} \right] \boldsymbol{n}_i^{n,A}, \tag{2.37}$$

in which, $\boldsymbol{f}_{i,norm}^{n+1,A}$ is the force applied at the body A in the direction normal to node i, and m_i^A is the corresponding mass of node i obtained for body A. Until now, the interpenetration of objects is prevented. The frictional traction is applied next. Assuming that the two bodies are sticking to each other, the force required for keeping them together is obtained from the tangential component of the relative velocity represented as

$$\boldsymbol{f}_{i,stick}^{n+1,A} = -\frac{m_i^{n,A}}{\Delta t}\boldsymbol{n}_i^{n,A} \times \left[\left(\tilde{\boldsymbol{v}}_i^{n+1,A} - \tilde{\boldsymbol{v}}_i^{n+1,(A+B)}\right) \times \boldsymbol{n}_i^{n,A}\right], \qquad (2.38)$$

where, $\boldsymbol{f}_{i,stick}^{n+1,A}$ is the tangential force required to hold the bodies glued together. To model frictional sliding, a limit for tangential forces following the formulation of Coulombs's friction law is defined. The tangential forces is represented by

$$\boldsymbol{f}_{i,tang}^A = \frac{\boldsymbol{f}_{i,stick}^A}{\|\boldsymbol{f}_{i,stick}^A\|}\min\left(\mu\|\boldsymbol{f}_{i,norm}^A\|, \|\boldsymbol{f}_{i,stick}^A\|\right), \qquad (2.39)$$

where, $\boldsymbol{f}_{i,tang}^A$ is the tangential component of the frictional contact force, and μ is the coefficient of friction. The forces considered in Equation 2.39 are obtained at the end of the time step.

2.6.3 State of the Art

In this thesis, the penalty function method, that is often used in FE formulations is implemented in CPDI, where the contact forces in the normal direction is assumed to be proportional to the residual of the impenetrability constraints and the surface stiffness. The surface of the continuum is discretised separately from the volume discretisation. By setting a certain amount of mass to the surface, the surface nodes are able to follow the deformation of the continuum. Upon the equation of motion, the surface nodes of individual entities might interact according to the penalty function. Frictional forces are then traced back as an external contact force acting on the boundary.
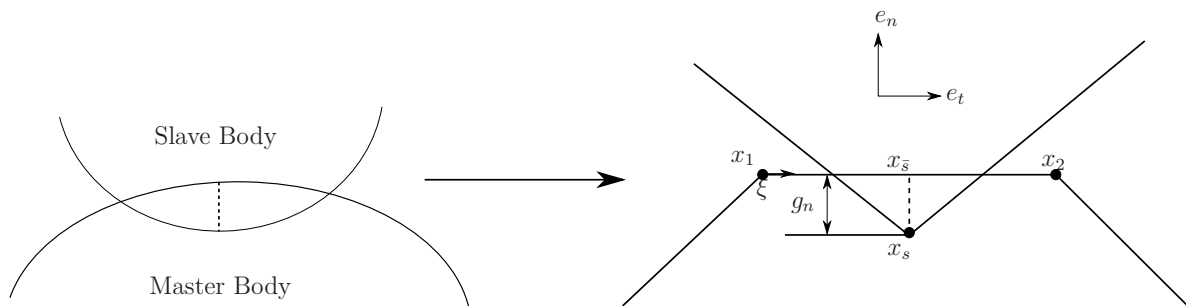
Figure 2.6: Penalty contact conditions

2.6.4 Penalty function method

Contact problems are formulated as a constrained optimisation problem. Numerical treatment of contact constraints are carried out by a variety of methods like sequential quadratic programming method, active set strategies and mathematical programming method. Solving a constrained optimisation problem is not trivial because of the requirement to build test functions that satisfy zero-displacement boundary conditions. Since the contact boundaries are not known before the problem is solved, it is not trivial to build the test functions either. It is therefore converted to an unconstrained optimisation problem by using the Lagrange multiplier method or the Penalty method. Although penalty method provides approximate solutions, it is widely used for its simplicity to satisfy the kinematic constraints in the weak sense. In this method, if a region Γ_c where contact violation exists on a body as shown in Figure 2.6, the potential energy is penalised proportional to the amount of constraint violation by using a penalty function P, and is expressed as

$$P = \frac{1}{2}\omega_n \int_{\Gamma_c} g_n^2 \, d\Gamma_c + \frac{1}{2}\omega_t \int_{\Gamma_c} g_t^2 \, d\Gamma_c \, , \tag{2.40}$$

where, ω is the penalty parameter, g is the gap function and the subscripts n and t refer to the normal and tangential directions, respectively. By adding Equation 2.40 to the total potential energy, the constrained minimisation problem is converted to an unconstrained minimisation problem. The contact variational form is obtained from Equation 2.40, which yields

$$\delta P \left(\boldsymbol{u}, \delta \boldsymbol{u} \right) = \omega_n \int_{\Gamma_c} g_n \, \delta g_n \, d\Gamma_c + \omega_t \int_{\Gamma_c} g_t \, \delta g_t \, d\Gamma_c \, , \tag{2.41}$$

where, $\boldsymbol{u}$ is the displacement vector and the symbol δ denotes the variation of a quantity. The gap functions g are defined as

$$g_n = \left(\boldsymbol{x}_s - \boldsymbol{x}_{\bar{s}} \right) \boldsymbol{e}_n^T \qquad \text{and} \qquad g_t = \|\boldsymbol{t}^0\| \left(\xi_{\bar{s}} - \xi_{\bar{s}}^0 \right) \, , \tag{2.42}$$

where, $\boldsymbol{x}_s$ is the position vector of the slave node s, $\bar{s}$ is the projection of s on the master segment, $\boldsymbol{e}_n$ is the unit vector in the normal direction, $\boldsymbol{t}$ being the tangential vector and the superscript 0 denotes the values at the previous time step. The natural coordinate ξ is defined as

$$\xi = \frac{1}{\|\boldsymbol{t}\|} \left(\boldsymbol{x}_s - \boldsymbol{x}_1 \right)^T \boldsymbol{e}_t \qquad \text{and} \qquad 0 \leq \xi \leq 1 \, , \tag{2.43}$$

where, $\boldsymbol{x}_1$ is the position vector of one of the master segments's ends and $\boldsymbol{e}_t$ is the unit vector in the tangential direction. Taking the variation of Equation 2.42 and back substituting the results to Equation 2.41 gives

$$\delta P\left(\boldsymbol{u}, \delta\boldsymbol{u}\right) = \omega_n \int_{\Gamma_c} g_n\, \boldsymbol{e}_n^T \left(\delta\boldsymbol{u}_s - \delta\boldsymbol{u}_{\bar{s}}\right)\, d\Gamma_c$$
$$+ \omega_t \int_{\Gamma_c} g_t\, \|\boldsymbol{t}^0\| \left(\frac{\|\boldsymbol{t}\|\, \boldsymbol{e}_t^T\left(\delta\boldsymbol{u}_s - \delta\boldsymbol{u}_{\bar{s}}\right) + g_n\, \boldsymbol{e}_n^T\, \delta\boldsymbol{u}_{\bar{s},\xi}}{\|\boldsymbol{t}\|^2 - g_n\, \boldsymbol{e}_n^T\, \boldsymbol{x}_{\bar{s},\xi\xi}}\right)\, d\Gamma_c\ . \tag{2.44}$$

Equation 2.44 is discretised to the form

$$\delta P(\boldsymbol{u}, \delta\boldsymbol{u}) \approx \sum_{i=1}^{ns} \delta\hat{\boldsymbol{u}}^T \left(\omega_n\, g_n\, \boldsymbol{C}_n + \omega_t\, g_t\, \boldsymbol{C}_t\right)_i\ , \tag{2.45}$$

where $\hat{\boldsymbol{u}}$ is the nodal displacement and ns is the number of slave nodes that penetrate into the master segments. $\boldsymbol{C}_n$ and $\boldsymbol{C}_t$ in Equation 2.45 read as [33, 52]

$$\boldsymbol{C}_n = \boldsymbol{N} - \frac{g_n}{l}\boldsymbol{Q}, \qquad \text{and} \qquad \boldsymbol{C}_t = \boldsymbol{T} + \frac{g_n}{l}\boldsymbol{P}\ , \tag{2.46}$$

with

$$\boldsymbol{u} = \begin{bmatrix} \boldsymbol{u}_s \\ \boldsymbol{u}_1 \\ \boldsymbol{u}_2 \end{bmatrix} \qquad \boldsymbol{N} = \begin{bmatrix} \boldsymbol{e}_n \\ -(1-\xi)\,\boldsymbol{e}_n \\ -\xi\,\boldsymbol{e}_n \end{bmatrix} \qquad \boldsymbol{T} = \begin{bmatrix} \boldsymbol{e}_t \\ -(1-\xi)\,\boldsymbol{e}_t \\ -\xi\,\boldsymbol{e}_t \end{bmatrix} \qquad \boldsymbol{P} = \begin{bmatrix} \boldsymbol{0} \\ -\boldsymbol{e}_n \\ \boldsymbol{e}_n \end{bmatrix} \qquad \boldsymbol{Q} = \begin{bmatrix} \boldsymbol{0} \\ -\boldsymbol{e}_t \\ \boldsymbol{e}_t \end{bmatrix}\ , \tag{2.47}$$

where $\boldsymbol{u}_1$ and $\boldsymbol{u}_2$ are the displacement of the two ends of the master element, which has the length l. The final frictional force on the master and slave nodes are written as

$$\boldsymbol{F}^{inter} = \sum_{i=1}^{ns} \left(\omega_n\, g_n\, \boldsymbol{C}_n + \omega_t\, g_t\, \boldsymbol{C}_t\right)\ , \tag{2.48}$$

in which $\boldsymbol{F}^{inter}$ is the assembly of interaction forces.

2.6.5 Contact Algorithm

Formulation of the improved contact algorithm is accomplished by reformulating the penalty function method in the framework of CPDI. For this purpose, an interface surface is defined along which the penalty function method is applied. The problems simulated are considered as two-dimensional. The surface is discretised using two-node linear segments. Thickness is also assigned to the segments so that mass is also allocated to the interface nodes according to the density of the continuum. In all cases, a thickness of less that 1% of the entity thickness is assumed. In addition to thickness, the normal and the tangential stiffness must also be specified. This can be same as the value of elastic stiffness to which the nodes are attached. Exceeding the maximum stiffness of the system will influence the stability of the

procedure. On the other hand, if a very low value of normal stiffness is assigned, penetration between entities during the solution procedure is likely. The coordinates, material properties, position, velocity and forces of the surface nodes and the material points are stored in separate databases. These are then tracked during the solution process for each node. In case the potential contact region is known before the simulation, a surface mesh can be assigned to only that region in order to reduce the computational effort. During the computation process, interface nodes follow the MPM algorithm and their location is updated using the velocity field obtained from the computational grid as elaborated in Section 2.5. After updating the locations, a detection for overlap of the surface nodes of different entities is then performed.

2.6.6 Definition of contact pair

When two bodies are in contact, the concept of master-slave distinguishes the bodies. Although there is no theoretical reason to distinguish one body from another, the distinction is made of numerical convenience. One body is defined as the master, while the other, the slave. Contact conditions are then imposed taking into consideration that the slave body cannot penetrate the master body. This implies that hypothetically, the master body can penetrate the slave body. This is not physically possible, but numerically possible because it is not checked. When a curved boundary with a fine mesh is selected as the master body, a straight slave boundary with a coarser mesh shows a significant amount of penetration, even if none of the slave nodes penetrate into the master body. It is important to make the definition of master-slave bodies in order to minimise the numerical error. In general, a flat and stiff body is selected as the master body, and curved/concave and softer body is selected as the slave. In addition, the body with a coarser mesh is selected as the master and the body with a finer mesh is selected as the slave.

2.6.7 Detection of Contact Pair

In classical MPM, the contact algorithm for multi-velocity fields that allows separation, rolling and sliding with Coulomb criterion is usually adopted [7, 23]. Contact between two bodies, A and B at a computational node i is activated if the following inequality is satisfied

$$\left(\boldsymbol{v}_i^A - \boldsymbol{v}_i^{A+B} \right) \cdot \boldsymbol{n}_i^A > 0 \; , \tag{2.49}$$

where, $\boldsymbol{n_i}$ denotes the outward unit normal at i. The superscripts A refers to the velocity when body A is considered by itself and $A + B$ corresponds to the velocity when bodies A and B are combined simultaneously. In addition to Equation 2.49, the surface traction $\boldsymbol{t} = \boldsymbol{\sigma} \cdot \boldsymbol{n}$ in the vicinity of i is required to be in compression. Using the condition in inequality 2.49 along with the CPDI concept, the two bodies interact if they contribute to the same computational node, implying a bigger gap between the interacting bodies than

that for the original MPM. Zheng et al. [72] suggests an additional criterion based on the updated particle domain

$$\left(\boldsymbol{x}_j^A - \boldsymbol{x}_k^B \right) \cdot \boldsymbol{n}_k^B \leq 0 \ , \tag{2.50}$$

where, $\boldsymbol{x}_j^A$ is the position of thee corner j corresponding to body A and $\boldsymbol{n}_k^B$ is the unit normal associated with the corner k of body B. Although Equation 2.50 is a refinement over the previous method, the iterative method required for detecting these particles is computationally expensive. Furthermore, implementing the above Equation results in numerical difficulties for the case of heavy-impact problems like pile-penetration and requires modifying the equation using geometric algebra, adding a new layer of complexity. A new method is therefore suggested for contact detection.

Detection of contact pairs is done in three steps. In the first step, it is checked whether the momenta of different interface discretisation contribute to the same computational node. Elements attached to this node are then tagged as a zone containing surface nodes that potentially might be in contact. Subsequent iterations will be carried out for the surface nodes that are located inside the tagged elements, which is usually much smaller than the total number of surface nodes. In the second step, the algorithm checks whether the distance between a node of an entity and another node of a different entity is smaller than the minimum search size. This minimum search size is usually the computational grid spacing, as for the explicit procedure being adopted, the propagating wave is restricted by the grid size during the time step. The final step of the algorithm is to identify node-segment pairs in the sub-group that is identified in the second step that satisfy the following condition

$$g_n < 0 \quad \text{and} \quad 0 \leq \xi \leq 1 \ , \tag{2.51}$$

where, the first condition checks whether the slave node has penetrated into the master segment and the second condition checks whether the slave node is within the space of the master element.

2.6.8 Calculation of contact forces

If a pair of master segment and slave node that are in contact is established from the search algorithm, the resisting force to oppose the penetration is calculated from Equation 2.48. Although a predictor-corrector procedure can be performed to improve the accuracy of nodal contact force, it can be avoided in explicit time stepping as the error in force estimation is assumed to be small. In order to couple the surface discretisation with the MPM solution, contact forces are mapped from the one-dimensional boundary to the four node computational mesh via

$$\boldsymbol{F}_i^{cont} = \sum_{j=1}^{nc} \boldsymbol{N}_i^j \boldsymbol{F}_j^{inter} \ , \tag{2.52}$$

where, $\boldsymbol{N}_i^j$ is the shape function of computational node i evaluated at the location of boundary node j, nc is the number of contact nodes and $\boldsymbol{F}_i^{cont}$ is the contact force expressed
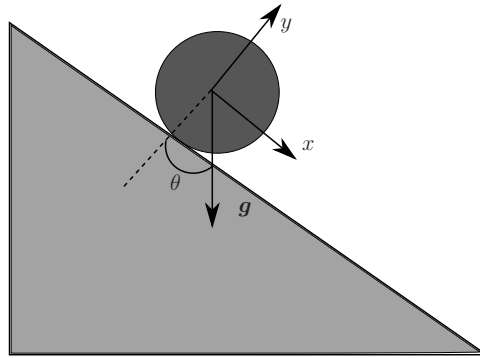
Figure 2.7: Schematic of the inclined plane problem

at the computational grid. Interaction of the bodies will contribute to the momentum equation through the additional quantity expressed as

$$M_i \boldsymbol{a}_i = \boldsymbol{F}^{ext} - \boldsymbol{F}^{int} + \boldsymbol{F}^{cont} \; , \tag{2.53}$$

where, M is the lumped mass, $\boldsymbol{a}$ the nodal acceleration, the subscript i refers to the grid node and $\boldsymbol{F}^{ext}$ and $\boldsymbol{F}^{int}$ the external and internal force vectors, respectively.

2.6.9 Verification of Penalty Contact Algorithm

To demonstrate the accuracy of the algorithm, numerical solutions are compared to analytical ones from rigid body dynamics. To verify the contact algorithm, a simple test is performed on the work of Bardenhagen et al. [8]. In the original work, a three-dimensional sphere rolling down an inclined plane, has been simulated. Owing to the present two-dimensional implementation, instead of a sphere, the problem of a cylinder rolling down an inclined plane is simulated. For the test performed, CPDI, an improved version of MPM is used, the same formulation that would be used in the later part of the Thesis for pile installation application.

Figure 2.7 provides the schematic of the problem setup. The radius of the cylinder is taken as 1.6m, and the length of the plane on which it rolls is modelled to be 20m long. A thickness of 0.8m is assigned to the plane. The inclination of the plane is described as the angle between the y-direction and that of gravity g, given by θ. The acceleration due to gravity is taken as 10 m/s^2 for all calculations.

In this simulation, the plane and the cylinder are both deformable. A plane-strain analysis using a four-node regular cell of 0.4m size is performed. An irregular CPDI discretisation is selected with overlapping domains, in which the maximum particle size is set as 0.2m. As mandated by the proposed penalty algorithm, an interface layer is modelled and discretised with a thickness of 0.001m, using two-node elements of size 0.1m. This yields a total of 517 linear segments. Discretisation of the sphere and plane is depicted in Figure 2.8. The
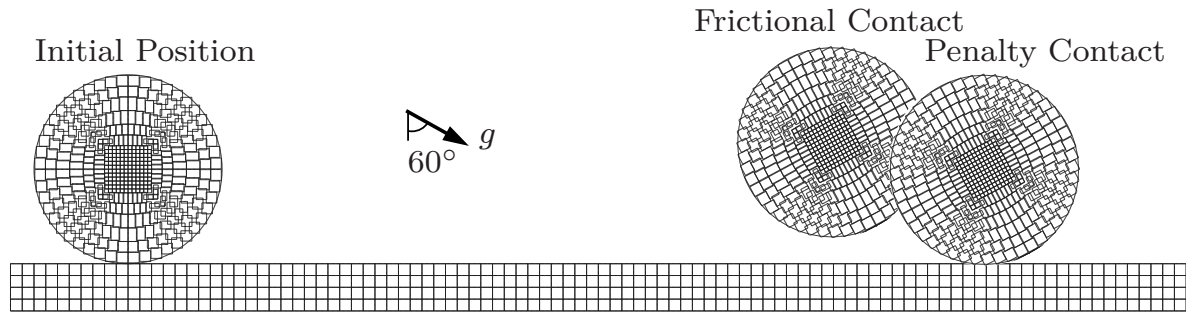
Figure 2.8: Discretisation of inclined plane problem

sphere and the plane are modelled as compressible Neo-hookean hyperelastic bodies. The cylinder has a bulk modulus of 6MPa, shear modulus of 3 MPa, and a density of 1000 kg/m^3. These value roughly approximate those of natural rubber. The plane follows the same elastic constants, but are multiplied by a factor of ten.

The tests are performed for two cases of inclination of plane. For the first case, the inclination angle $\theta = \pi/4$, and the coefficient of friction is 0.495. This case is referred *no-slip* case, as the rigid cylinder solution describes rolling without slipping. The position of centre of mass for the rigid cylinder for this case is given by

$$x(t) = \frac{5\sqrt{2}}{3} t^2, \tag{2.54}$$

where, x describes the position along the plane at time t. The position of centre of mass and the velocity for the *no-slip* and the velocity, are depicted in Figures 2.9 and 2.10, respectively.
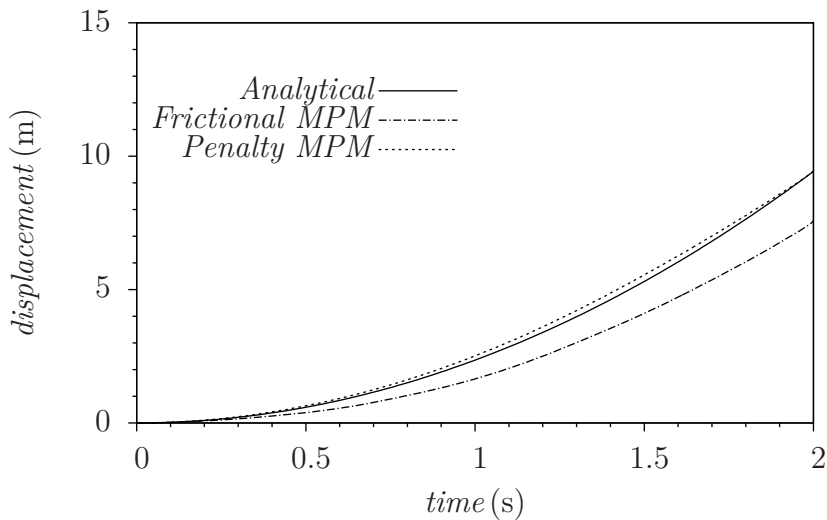

Figure 2.9: Displacement of the centre point of the rolling cylinder for no-slip case
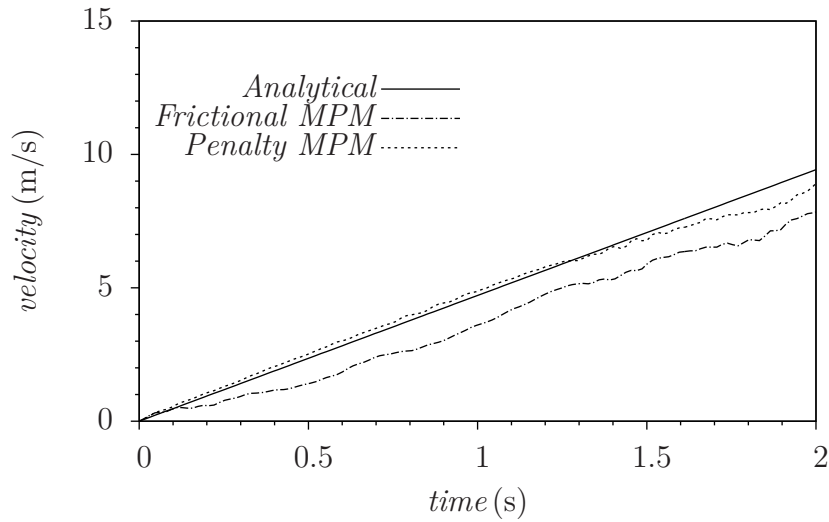
Figure 2.10: Velocity of the centre point of the rolling cylinder for no-slip case

For the second case, the inclination angle is set at $\theta = \pi/3$, and the corresponding coefficient of friction is set as 0.286. In this case, the analytical solution describes rolling while sliding, and is referred to as the *slip* case. For a rigid cylinder, the position of centre of mass is given by

$$x(t) = \frac{5}{2} \left(\sqrt{3} - \frac{2}{7} \right) \ t^2. \tag{2.55}$$

The displacement and the velocity for the *slip* case is depicted in Figures 2.11 and 2.12, respectively.
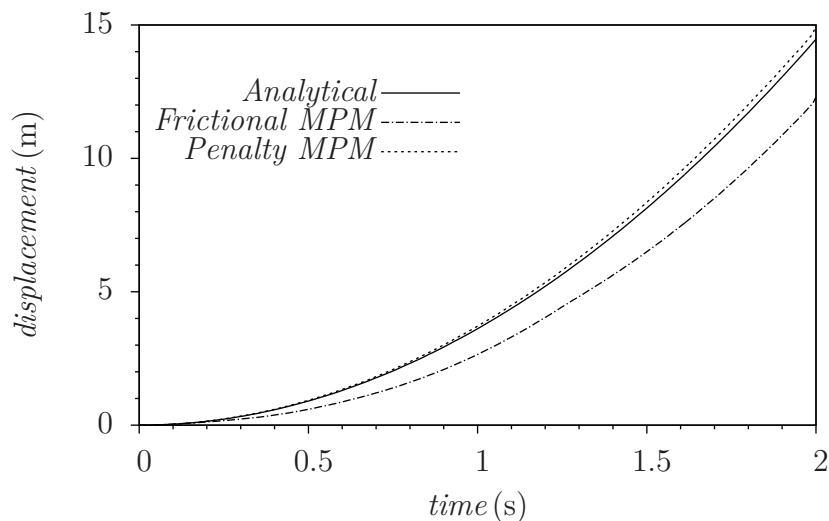

Figure 2.11: Displacement of the centre point of the rolling cylinder for slip case
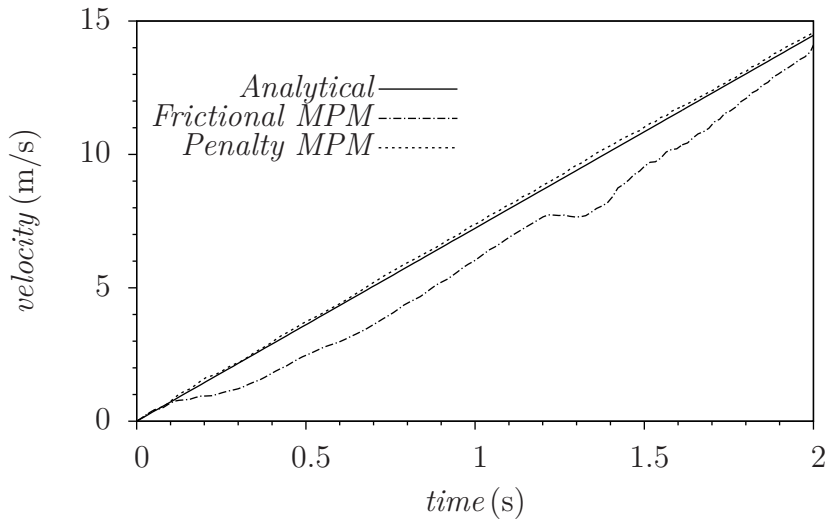
Figure 2.12: Velocity of the centre point of the rolling cylinder for slip case

For the simulation of both cases, the initial gravity stresses are evaluated at zero inclination. The plane and the cylinder are then suddenly tilted. In all Figures, the proposed method along with Frictional contact algorithm is depicted for the purpose of comparison. It is evident that the results obtained from the proposed penalty contact algorithm are in closer agreement to the analytical solution than the frictional contact algorithm. The slower motion in the frictional MPM contact is attributed to the initial position of the two bodies between which no gap is assumed. In the formulation of frictional contact, the interaction between the material points is initiated within the influence of one computational grid. Resistance force is therefore overestimated until a gap is formed. This is illustrated in Figure 2.8. It is observed from Figures 2.10 and 2.12 that although the velocity in both slip and no-slip cases matches the analytical value in the beginning, the frictional contact algorithm fails to represent the linear variation in velocity. The proposed penalty contact algorithm represents the linear variation in velocity throughout the simulation, except in the last part of the no-slip case (see Figure 2.10). The position of centre of mass for the frictional contact algorithm does not match the analytical value exactly in both the cases (see Figures 2.9, 2.11). This is attributed to the overestimation of contact force between the bodies. In case of the proposed penalty contact however, the difference between the analytical and numerical values are negligible.

Chapter 3

Soil Modelling

3.1 Introduction

Constitutive modelling of natural structured sand has observed significant developments in the past years in order to accurately reproduce soil behaviour. Mechanical behaviour of granular soils, ranging from silt to gravel, can be modelled by different theories. Hypoplasticity, a constitutive theory suitable for modelling behaviour of frictional materials is originally developed for granular materials like sand and gravel [65, 68]. Contrary to elastoplasticity, no distinction of elastic and plastic deformation, yield and plastic potential surfaces or hardening rules are needed.

Modifications have since been carried out for fine-grained soil in several works. Niemunis [48] develops a rate-independent visco-hypoplastic model as a combination of hypoplasticity with modified cam-clay yield conditions. Niemunis et al. [49] in his work further enhances the model by the effects of strength anisotropy and irreversibility of the response within the state boundary surface. Franzius et al. [20] demonstrates that improved predictions are obtained in tunnelling problems by incorporating stiffness anisotropy. Herle and Kolymbas [28] made modifications to the model proposed by von Wolffersdorff [65] in order to predict the rate-independent behaviour of soils with low friction angles. This model is later refined by Mašín [44] by reducing the number of parameters, and by considering the asymptotic states which is a better representation of fine-grained soil behaviour. Subsequently, Weifner and Kolymbas [66] develops a hypoplastic model capable of simulating the behaviour of both sand and clay.

Hypoplasticity in its basic form cannot accurately predict the soil behaviour in small to very small strain range. It is therefore unsuitable for predicting cyclic soil response. To overcome this shortcoming, the model is extended and one of the approaches taken is for the model to be combined with the intergranular strain concept [47], where the small strain stiffness is also accounted for in the model by introducing an additional variable intergranular strain. In this thesis, the model proposed by von Wolffersdorff [65] has been used along with its extension to small strain stiffness along the work of Niemunis and Herle [47].

3.2 Hypoplastic model for Sand

This section presents a brief overview of the hypoplastic model for sand and its extension to small strain stiffness. The material model of sand is based on the work of von Wolffersdorff [65] and its extension to small strain stiffness, on the work of Niemunis and Herle [47].

3.2.1 Model Formulation

Hypoplasticity is an approach to non-linear constitutive modelling of geo-materials. Following from von Wolffersdorff [65], the hypoplastic constitutive relation in the rate form is expressed as

$$\dot{\boldsymbol{\sigma}} = \boldsymbol{G}\ (\boldsymbol{\sigma}, e, \dot{\boldsymbol{\epsilon}}), \tag{3.1}$$

where, $\dot{\boldsymbol{\sigma}}$ is the Zareba-Jaumann stress rate tensor, $\dot{\boldsymbol{\epsilon}}$ is the strain rate tensor, and e is the current void ratio. The rate of void ratio is follows from

$$\dot{e} = (1+e)\ tr\,(\boldsymbol{\epsilon}). \tag{3.2}$$

The general form of the tensorial function $\boldsymbol{G}$ is selected such that

$$\dot{\boldsymbol{\sigma}} = \boldsymbol{L}\dot{\boldsymbol{\epsilon}} + \boldsymbol{N}\|\dot{\boldsymbol{\epsilon}}\|, \tag{3.3}$$

where, $\boldsymbol{L}$ and $\boldsymbol{N}$ are the fourth-order linear and second-order non-linear constitutive tensors, respectively. The term $\|\dot{\boldsymbol{\epsilon}}\|$ is the Euclidean norm of the strain rate tensor. For ease of representation, Equation 3.3 is represented in index notation as

$$\dot{\sigma_{ij}} = L_{ijkl}\dot{\epsilon_{kl}} + N_{ij}\sqrt{\dot{\epsilon_{ij}\epsilon_{ij}}}, \tag{3.4}$$

with L_{ijkl} and N_{ij} being the linear and non-linear constitutive tensors, respectively. The decomposition of function $\boldsymbol{G}$ into a linear and non-linear tensors is performed to achieve the inelastic behaviour of sand without having to decompose the strain into elastic and plastic parts. Tensors L_{ijkl} and N_{ij} are functions of stress and void ratio. They are represented as

$$L_{ijkl} = f_b\ f_e \frac{1}{\hat{\sigma}_{ij}\hat{\sigma}_{ij}}\left(f^2\ \delta_{ik}\ \delta_{jl} + a^2\ \hat{\sigma}_{ik}\ \hat{\sigma}_{jl}\right), \tag{3.5}$$

$$N_{ij} = f_d\ f_b\ f_e \frac{af}{\hat{\sigma}_{ij}\hat{\sigma}_{ij}}\left(\hat{\sigma}_{ij} + \hat{\hat{\sigma}}_{ij}\right). \tag{3.6}$$

The tensors $\hat{\sigma}_{ij}$ and $\hat{\hat{\sigma}}_{ij}$ are the normalised stress tensor and the deviatoric stress tensor, respectively. They are represented as

$$\hat{\sigma}_{ij} = \frac{\sigma_{ij}}{I_1}, \quad \text{with} \quad I_1 = \sigma_{11} + \sigma_{22} + \sigma_{33}, \tag{3.7}$$

$$\hat{\hat{\sigma}}_{ij} = \hat{\sigma}_{ij} - \frac{1}{3}\delta_{ij}. \tag{3.8}$$
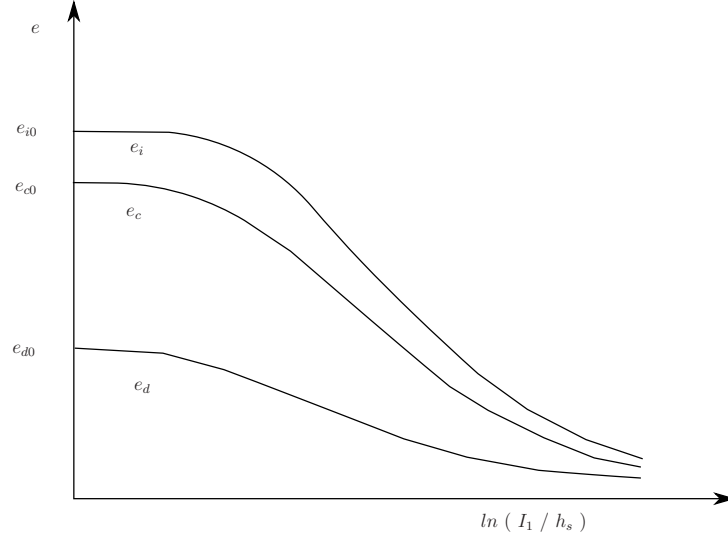
Figure 3.1: Characteristic void ratios as a function of stress[65]

From Equation 3.5, the constant a is represented as

$$a = \frac{\sqrt{3}\ (3 - \sin\phi_c)}{2\ \sqrt{2}\ \sin\phi_c},$$

(3.9)

where ϕ_c is the critical state friction angle, and the factor f is represented as

$$f = \sqrt{\frac{1}{8}\tan^2\psi + \frac{2 - \tan^2\psi}{2 + \sqrt{2}\ \tan\psi\ \cos 3\theta}} - \frac{1}{2\sqrt{2}}\tan\psi,$$

(3.10)

where, $\cos 3\theta$ is the Lode angle function and is given by

$$\cos 3\theta = -\sqrt{6}\ \frac{\text{tr}(\hat{\hat{\boldsymbol{\sigma}}} \cdot \hat{\hat{\boldsymbol{\sigma}}} \cdot \hat{\hat{\boldsymbol{\sigma}}})}{\left[\hat{\hat{\boldsymbol{\sigma}}} : \hat{\hat{\boldsymbol{\sigma}}}\right]^{3/2}}\ .$$

(3.11)

$\tan\psi$ is defined as

$$\tan\psi = \sqrt{3}\ \|\hat{\hat{\boldsymbol{\sigma}}}\|\ .$$

(3.12)

We define three characteristic void ratios namely, critical void ratio e_c, the minimum possible void ratio e_d corrected to the corresponding density, and the maximum possible void ratio e_i corresponding to the minimum density. The variables e_{c0}, e_{d0} and e_{i0} correspond to the void ratios at vanishing pressure represented by the first stress invariant I_1. The range of possible void ratios are a function of stress is represented in Figure 3.1. From Equation 3.6, the factors f_e and f_d are represented as

$$f_e = \left(\frac{e_c}{e}\right)^\beta, \quad \text{and} \quad f_d = \left(\frac{e - e_d}{e_c - e_d}\right)^\alpha$$

(3.13)

with β and α being the input indices. From Equation 3.5, the pressure dependency of the soil stiffness, represented by the factor f_b is defined as

$$f_b = \frac{h_s}{n}\left(\frac{1 + e_i}{e_i}\right)\left(\frac{e_{i0}}{e_{c0}}\right)^\beta\left(\frac{-I_1}{h_s}\right)^{1-n}\left[3 + a^2 - \sqrt{3}\,a\left(\frac{e_{i0} - e_{d0}}{e_{c0} - e_{d0}}\right)^\alpha\right]^{-1},$$

(3.14)

where, h_s is the pressure independent granular stiffness and n is an input index. The characteristic void ratios are updated according to the relation

$$\frac{e_i}{e_{i0}} = \frac{e_c}{e_{c0}} = \frac{e_d}{e_{d0}} = \exp\left[-\left(\frac{-I_1}{h_s}\right)^n\right].$$

(3.15)

Finally, substituting Equations 3.5 and 3.6 into Equation 3.4, the final constitutive equation is expressed as

$$\dot{\sigma}_{ij} = f_b f_e \frac{1}{\hat{\sigma}_{ij}\hat{\sigma}_{ij}} \left[f^2 \dot{\epsilon}_{ij} + a^2 \left(\hat{\sigma}_{ik}\hat{\sigma}_{jl}\right)\dot{\epsilon}_{kl} + a f f_d \left(\hat{\sigma}_{ij} + \hat{\hat{\sigma}}_{ij}\right)\sqrt{\dot{\epsilon}_{ij}\dot{\epsilon}_{ij}}\right]$$

(3.16)

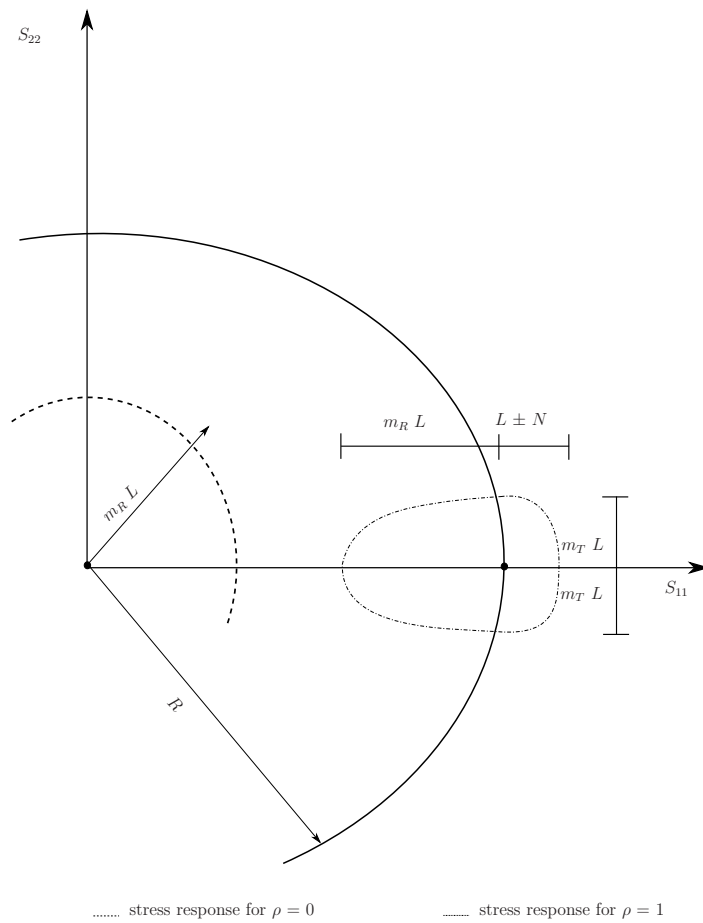........ stress response for $\rho = 0$ .... stress response for $\rho = 1$

Figure 3.2: Stiffness dependency on m_r and m_T for the two ρ values[65]

3.2.2 Extension to small strain stiffness

To predict the very small strain stiffness and recent stress history effects, the model is combined with the intergranular strain concept [47]. The formulation is extended to account for small strain stiffness, by introducing a new state variable called the intergranular strain $\boldsymbol{\delta}$ denoted by

$$\boldsymbol{\delta} = \int \dot{\boldsymbol{\delta}} dt \ , \tag{3.17}$$

where,

$$\dot{\boldsymbol{\delta}} = \begin{cases} (\boldsymbol{I} - \hat{\boldsymbol{\delta}} \otimes \hat{\boldsymbol{\delta}} \rho^{\beta_r}) : \dot{\boldsymbol{\epsilon}}, & \text{for } \hat{\boldsymbol{\delta}} : \dot{\boldsymbol{\epsilon}} > 0 \\ \dot{\boldsymbol{\epsilon}}, & \text{for } \hat{\boldsymbol{\delta}} : \dot{\boldsymbol{\epsilon}} \leq 0 \ , \end{cases} \tag{3.18}$$

with, $\hat{\boldsymbol{\delta}}$ being the direction tensor for the intergranular strain. It is defined as

$$\hat{\boldsymbol{\delta}} = \begin{cases} \boldsymbol{\delta}/\|\boldsymbol{\delta}\|, & \text{for } \boldsymbol{\delta} \neq \mathbf{0} \\ \mathbf{0}, & \text{for } \boldsymbol{\delta} = \mathbf{0} \ . \end{cases} \tag{3.19}$$

ρ is defined as the normalised intergranular strain magnitude defined as

$$\rho = \frac{\|\boldsymbol{\delta}\|}{R} \ . \tag{3.20}$$

β_r and R are intergranular strain concept parameters. The constitutive relation of the extended hypoplastic model is written as

$$\overset{\circ}{\boldsymbol{\sigma}} = \boldsymbol{M} : \dot{\boldsymbol{\epsilon}} \ . \tag{3.21}$$

The stiffness tensor of the intergranular strain concept formulation $\boldsymbol{M}$ is constructed from tensors $\boldsymbol{L}$ and $\boldsymbol{N}$ and is modified by two scalars m_T and m_R. The tensor is represented as

$$\begin{aligned} \boldsymbol{M} = & \left[\rho^\chi m_T + (1 - \rho^\chi) \, m_R\right] \boldsymbol{L} \\ & + \begin{cases} \rho^\chi (1 - m_T) \, \boldsymbol{L} : \hat{\boldsymbol{\delta}} \otimes \hat{\boldsymbol{\delta}} + \rho^\chi \boldsymbol{N} \hat{\boldsymbol{\delta}}, & \text{for } \hat{\boldsymbol{\delta}} : \dot{\boldsymbol{\epsilon}} > 0 \ , \\ \rho^\chi (m_R - m_T) \, \boldsymbol{L} : \hat{\boldsymbol{\delta}} \otimes \hat{\boldsymbol{\delta}}, & \text{for } \hat{\boldsymbol{\delta}} : \dot{\boldsymbol{\epsilon}} \leq 0 \ . \end{cases} \end{aligned} \tag{3.22}$$

In index notation, Equation 3.22 is written as

$$\begin{aligned} M_{ijkl} = & \left[\rho^\chi m_T + (1 - \rho^\chi) \, m_R\right] L_{ijkl} \\ & + \begin{cases} \rho^\chi (1 - m_T) \, L_{ijmn} \left(\hat{\delta}_{mk} \hat{\delta}_{nl}\right) + \rho^\chi N_{ik} \hat{\delta}_{jl}, & \text{for } \hat{\delta}_{ij} \dot{\epsilon}_{ij} > 0 \ , \\ \rho^\chi (m_R - m_T) \, L_{ijmn} \hat{\delta}_{mk} \hat{\delta}_{nl}, & \text{for } \hat{\delta}_{ij} \dot{\epsilon}_{ij} \leq 0 \ , \end{cases} \end{aligned} \tag{3.23}$$

with, variables m_R and m_T defined as

$$m_R = p_r A_g \left(\frac{p}{p_r}\right)^{n_g} \frac{4 A_m \alpha_G}{2 p \alpha_E} \left(\frac{\lambda^* \kappa^*}{\lambda^* + \kappa^*}\right) \frac{1}{\left(1 - \nu_{pp} - 2 \frac{\alpha_E}{\alpha_\nu^2} \nu_{pp}^2\right)} \ , \tag{3.24}$$

$$m_T = m_{rat} \, m_R. \tag{3.25}$$

The variables m_R and m_T depend on ρ as shown in Figure 3.2. Variables χ and m_{rat} are the intergranular strain concept parameters. A_g and n_g are parameters quantifying the dependency of shear modulus at very small strain on mean effective stress parameter.

3.2.3 Constrained Modulus Calculation

For the MPM formulation, time integration of momentum equation is restricted by the CFL (Courant, Friedrichs and Lewy) condition where the critical time step is bound by the characteristic length of the element and the wave speed of the material. This condition requires the constrained modulus E^c to calculate the wave speed and ultimately, the size of critical time step. We consider the case of one-dimensional straining similar to that of oedometer test. We take all the components in the strain rate tensor equal to zero except $\dot{\epsilon}_{22}$. For the sake of simplicity, the stresses are assumed to be isotropic and are given by

$$\hat{\sigma}_{ij} = \frac{1}{3}\delta_{ij}, \quad \text{and} \quad \hat{\dot{\sigma}}_{ij} = 0. \tag{3.26}$$

The above values are obtained given that $\hat{\sigma}_{ij}\hat{\sigma}_{ij} = \frac{1}{3}$. Given these conditions, and with $\psi = 0$ and $f = 1$, it is shown that

$$L = f_b \ f_e \left(3 + \frac{a^2}{3}\right), \text{and} \tag{3.27}$$

$$N = a \ f_b \ f_d \ f_e \tag{3.28}$$

With L and N being the components of the tensor L_{ijkl} and N_{ij}, respectively. This corresponds to $\dot{\epsilon}_{22} \neq 0$. The constrained modulus thus becomes

$$E^c = L \mp N, \tag{3.29}$$

with the minus and plus sign indicating the loading and unloading conditions, respectively. This yields the constrained modulus

$$E^c = [\rho^\chi m_T + (1 - \rho^\chi)\, m_R]\, L$$
$$+ \begin{cases} \rho^\chi (1 - m_T)\, L + \rho^\chi N, & \text{for } \hat{\delta}_{ij}\dot{\epsilon}_{ij} > 0 \ , \\ \rho^\chi (m_R - m_T)\, L, & \text{for } \hat{\delta}_{ij}\dot{\epsilon}_{ij} \leq 0 \ . \end{cases} \tag{3.30}$$

3.3 Model verification - Element test and Footing Problem

To validate the FORTRAN implementation of the model, a compression test similar to biaxial test for the sand model is performed. Triaxial test is a common method to measure the mechanical properties of deformable solids, especially soil, rock and other granular materials. Plane-strain biaxial test on the other hand, is not commonly performed in soil mechanics laboratory tests, as they are more complex compared to triaxial tests. Due to the formulation of the finite element code, which supports two-dimensional test, this test is performed. The numerical validation of the soil model is carried out assuming drained condition.
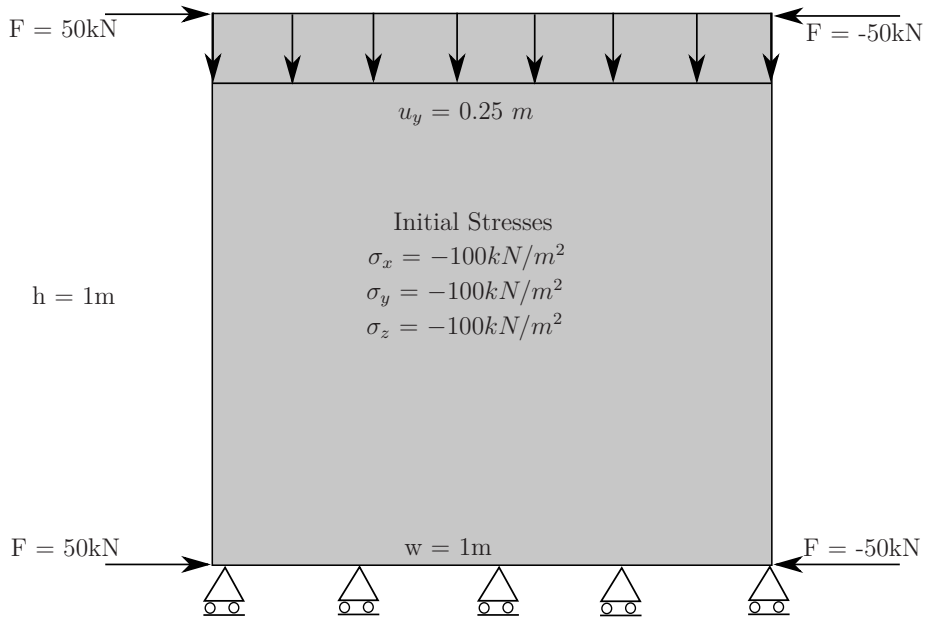
Figure 3.3: Initial configuration for soil compression test

A schematic representation of the initial configuration is represented in Figure 3.3. A material of width and height of 1m, respectively, is supported by roller supports at the bottom and a force of 50kN is applied on both the left and right nodes of the element. An initial uniform stress field is applied of $\sigma_x = \sigma_y = \sigma_z = -100kN/m^2$ is applied to the material initially. A prescribed displacement is then provided in the vertical direction from the top of the material. The material parameters used for both the tests used in the FE program and PLAXIS is tabulated in Table 3.1.

Variable	Value	Variable	Value
ϕ_c	30°	α	0.13
p_t	1.6	β	1.0
h_s	5.8E6	m_R	10.0
n	0.28	m_T	2.0
e_{d0}	0.53	R	5.0E-5
e_{c0}	0.84	β_r	0.3
e_{i0}	1.0	χ	1.0
e_0	0.65		

Table 3.1: Material properties for constitutive model for sand

The result of the test can be observed in Figure 3.4, where the comparison of results between FEM and PLAXIS under similar conditions is plotted. From the graph it is observed that the material model's Fortran implementation performs reasonably well, and yield results close to the ones obtained from the Plaxis element test. It is observed that the usage of the material model in finite element code would thus yield satisfactory results.
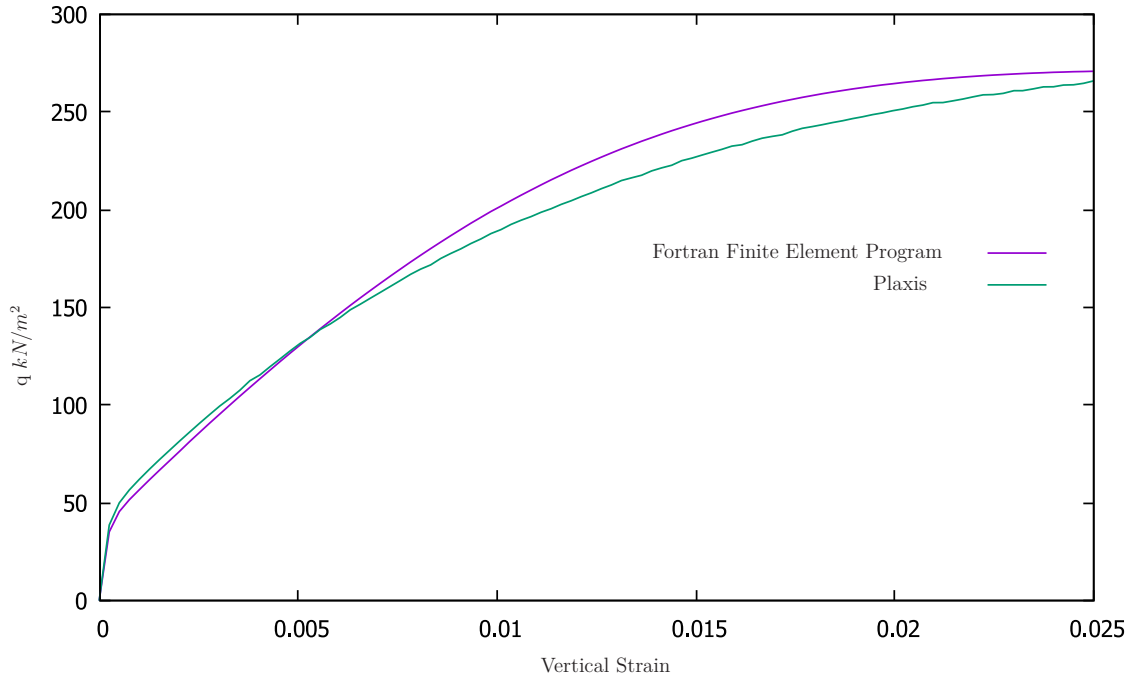

Figure 3.4: Deviatoric stress response over vertical strain application

Chapter 4

Pile Penetration

4.1 Introduction

Pile driving is an installation method practised in the field of offshore foundation engineering. The fundamental aspects of pile analyses still rely on empirical correlations based on experimental observations from laboratory and full scale in-situ testing [54]. The investigations are often carried out using instrumented piles allowing for a direct quantification of the base pressure and the shaft friction. Conventional FE method is traditionally used to predict the behaviour of pile and the soil [43]. As the simulation of pile driving involves large deformation, this causes mesh entanglement due to extreme mesh distortion. Among the alternates to FEM, MPM is widely used to simulate large deformation, and hence is used to simulate the problem of pile penetration.

A one-dimensional wave equation model for pile-driving analysis, in which the pile is represented by discrete elements and the soil, by a series of springs and dashpots is presented by Lee et al. [34]. This method though was widely used, the results were not accurate enough due to the one-dimensional approximation of the soil response. For realistic prediction of soil and pile behaviour, a three-dimensional or axi-symmetric analysis is required to capture the stress waves being transferred from the pile to the soil, and to properly model the interaction between the pile and soil.

Smith and Chow [57] performs a axi-symmetric simulation of pile driving in clay. A considerable difference in results is reported in comparison to the one-dimensional analysis. Mabsout and Tassoulas [43] performs a detailed analysis of pile driving using finite element technique. A non-linear axi-symmetric solution is developed, taking into account the large deformations that occur in the soil during the course of pile-driving. Bounding surface plasticity is adopted to model the inelastic behaviour of clay, with a frictional contact algorithm to characterize the interaction between pile and the clay. Transmitting boundaries are added to the soil in the far field boundaries to absorb the radiating waves resulting from the driving blow of the hammer. The hammer blow is simulated by a transient forcing function applied at the top of pile. Henke and Grabe [27] analyses different methods of pile driving like pile-jacking and vibratory pile driving. The influence of pile driving on adjacent

structures is also examined [26].

As an alternate to FEM, MPM is introduced and successfully applied in geotechnical applications such as cone penetration [10], pile penetration simulation [38] and spudcan simulation into the seabed [37].

4.2 Modelling pile installation

In this section, the installation of a pile being driven into a hypoplastic model of sand is simulated. The focus is investigation of the performance of the proposed penalty contact algorithm in the framework and CPDI, and compare the results with a similar simulation carried out in ABAQUS.

4.2.1 Dimensions and Parameters

The modelling of the pile is carried out as an axi-symmetric finite element problem. This modelling technique is justified by the assumption of vertical penetration of pile. A schematic of the problem is presented in Figure 4.1. In this section, two pile installation problems are modelled, one making use of the conventional frictional MPM contact, and the other in which the penalty contact method is implemented. The dimensions and material properties of both these cases are similar, barring the contact algorithm.

For the initialisation of the problem, a 10 X 5 m axisymmetric soil domain is assumed. The constitutive model for the soil is chosen as hypoplastic sand, whose numerical formulation is extensively explained in Chapter 3. The density of the soil is taken as $\rho_s = 2600 kg/m^3$. An initial void ratio of 0.65 is assumed for the soil. This represents now a dense sand. The material parameters of the soil are given in Table 4.1.

The pile is modelled as an elastic entity with a high modulus of elasticity. It is assumed to be 5m in length with a radius of 0.15m and the tip of the pile is rounded. The pile is initially placed on the surface of the soil. The pile is assigned an elastic modulus of 100MPa and a Poissons's ratio of 0.28. A density of $\rho_p = 2500 kg/m^3$ is assigned to the pile. A low stiffness is assigned to the pile in order to aid in speeding up the computation. Globally, the gravitational acceleration is rounded off to 10 m/s^2 and is assigned to the system.
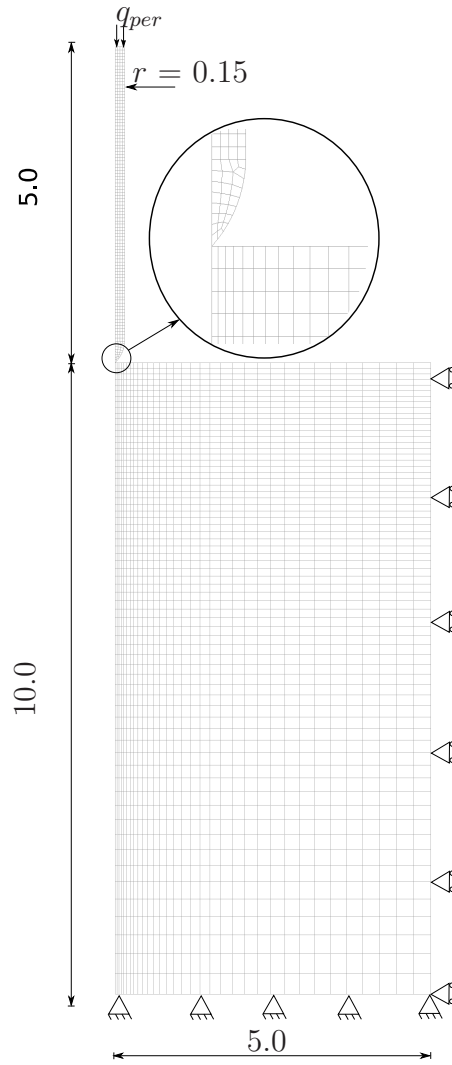
Figure 4.1: Dimensions and Mesh of Pile and Sand Assembly

Variable	Value	Variable	Value
ϕ_c	30°	α	0.13
p_t	1.6	β	1.0
h_s	5.8E6	m_R	10.0
n	0.28	m_T	2.0
e_{d0}	0.53	R	5.0E-5
e_{c0}	0.84	β_r	0.3
e_{i0}	1.0	χ	1.0
e_0	0.65		

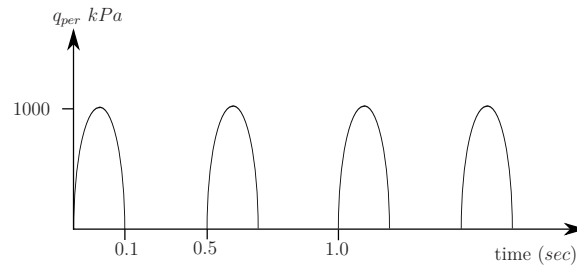Table 4.1: Hypoplastic sand model parameters

Figure 4.2: Time period of blows

4.2.2 Boundary Conditions

On the bottom of the domain, a fully fixed boundary condition is imposed, and along the vertical boundary on the outer edge, roller supports are imposed. Hamad [23] in his work notes that roller supports may be applied to the inner edge as well, but it does not have any impact on the outcome of the result. A friction coefficient of $\mu = 0.2$ is assigned for contact in case of both the classical frictional contact and penalty contact. A periodic load of 1000 kN/m^2 for a duration of 0.1 sec is applied on the top of the pile 4.2. The period of hammer blow is 0.5 sec. The simulation is carried out for a total of 12 seconds, 2 seconds for gravity loading and 10 seconds for dynamic loading.

4.2.3 Meshing

The 2D axisymmetric model is prepared in GiD preprocessor with a computational mesh size of 0.125 cm, containing a total of 10,432 particles, and for the case of Penalty contact algorithm, an additional 528 two-node elements are meshed. A total of 3,444 elements are meshed for the background computational mesh. A regular four-node quadrilateral discretisation is adopted for the computational mesh. In order to refine the number of material points near the pile, a non-regular distribution of material points is implemented. As a result, overlapping rectangles and squares of initial particle domain is observed near the tip of the pile, as shown in Figure 4.3. This overlaps, however, is avoided for the regular soil domain. Using this procedure, particle size can be as big as two computational elements in the zone where there is little variation. This aids in saving computational time.

For the treatment of penalty contact, an additional two-node linear segments are modelled to handle the contact between two bodies. A thickness of less than 1% of entity thickness is usually assumed, in this case a thickness of 0.001m is assigned to both the pile and the soil interface element. In addition to thickness, normal and tangential stiffness is also assigned to the elements. This can take the same value as the elastic stiffness where the nodes are attached, in this case, 100MPa is assigned. It must be noted that exceeding the maximum stiffness of the system would affect the stability of the explicit integration procedure. Conversely, penetration might occur if the normal stiffness is reduced excessively.
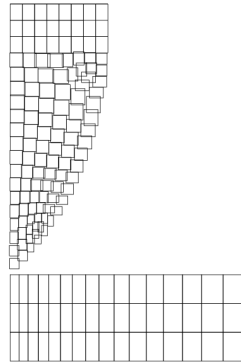
Figure 4.3: Overlap of particle domains near the tip

Figure 4.4 shows the additional interface element introduced in the case of penalty contact. It is to be noted that the interface element is modelled in areas where there potentially will be contact and not modelled throughout the model, as the potential contact zone is known apriori.

Once the boundary conditions are specified, and the model meshed, the model is then solved. The model is solved in a total of two phases, a gravity loading phase and the dynamic loading phase. In the gravity loading phase, the gravity load is applied gradually over a time period of two seconds. Once the gravity stresses have been obtained, the pile is then hammered into the soil by activating the dynamic traction load q_{per} (Figure 4.2).

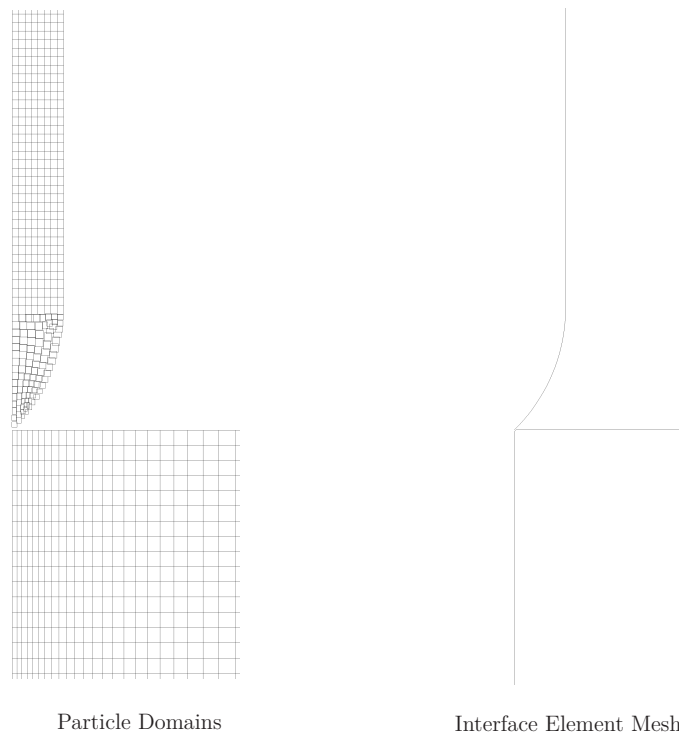Particle Domains   Interface Element Mesh

Figure 4.4: Interface element mesh for the corresponding particle domains

To obtain reference solution, as stated previously, a commercial FE package ABAQUS is used. To simulate large deformation during pile installation, the standard FE formulation will not be helpful. Instead, a *Coupled Eulerian-Lagrangian* approach is adopted. While modelling the installation process in ABAQUS, the pile is assumed to rigid, hence the pile is assigned as analytically rigid, thus becoming the Lagrangian part. For modelling the soil, a two step approach is followed. First, the soil body is created as a Lagrangian part. Subsequently, an Eulerian part, slightly bigger at the surface of the soil is created. This additional area is created to accommodate soil heaving during the pile installation process. The volume fraction to the Eulerian body is assigned to the extent of the Lagrangian body, and thereafter the Lagrangian soil part is suppressed. Material data is then assigned to the Eulerian soil part, the rigid pile along with the soil is then assembled, after assigning appropriate displacement and traction boundary conditions.

4.3 Results and Comparison

In this section, results have been compared to show the difference between the classical frictional MPM contact and penalty contact. In addition to MPM calculations, a simulation in ABAQUS is also carried out to draw comparisons between the results. The pile installation simulation in classical MPM formulation is comparable to the formulation elaborated by Hamad [23].

Initially, gravity stresses are built up gradually over a time period of 2 seconds. At the end of gravity loading step, a penetration depth of 0.25m is obtained for the case of classical frictional contact, as opposed to a penetration depth of 0.37m for the penalty contact algorithm. Due to the frictional contact algorithm overestimating the resistance force, a lower penetration is obtained in this case.

At the end of the gravity loading step, a vertical stress of -170 kN/m^2 is obtained. Figure 4.5 represents the stress distribution in soil and pile assembly in both the MPM calculations, as well as from the ABAQUS simulation. In classical frictional MPM contact, the stress oscillation at the tip is affected by refinement of the contact interface. It is also to be noted that the stress oscillation in the penalty contact algorithm is less pronounced as compared to the classical contact algorithm.
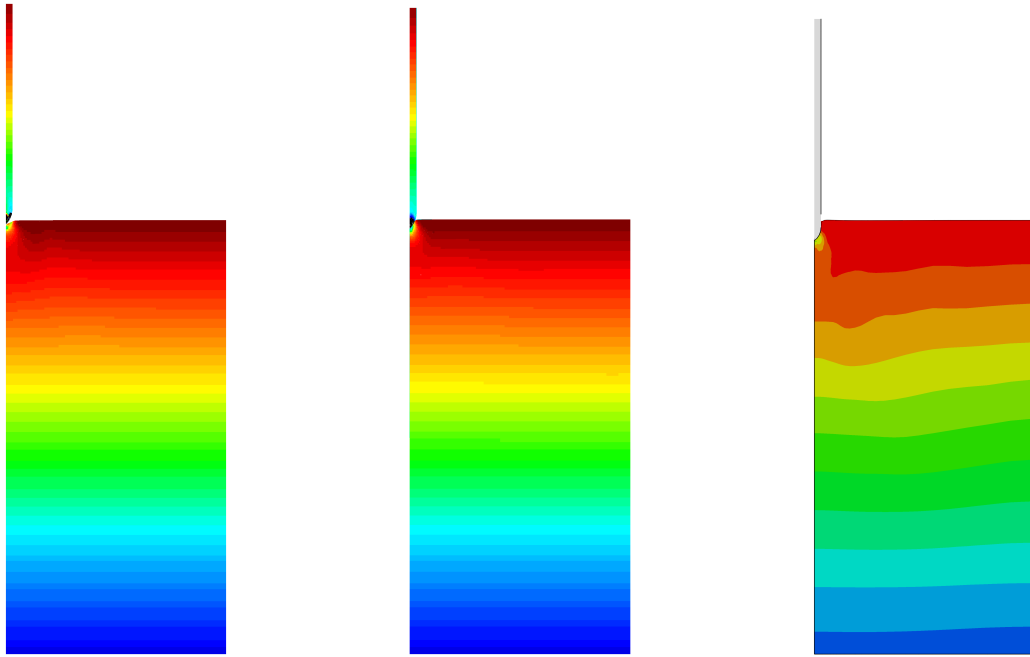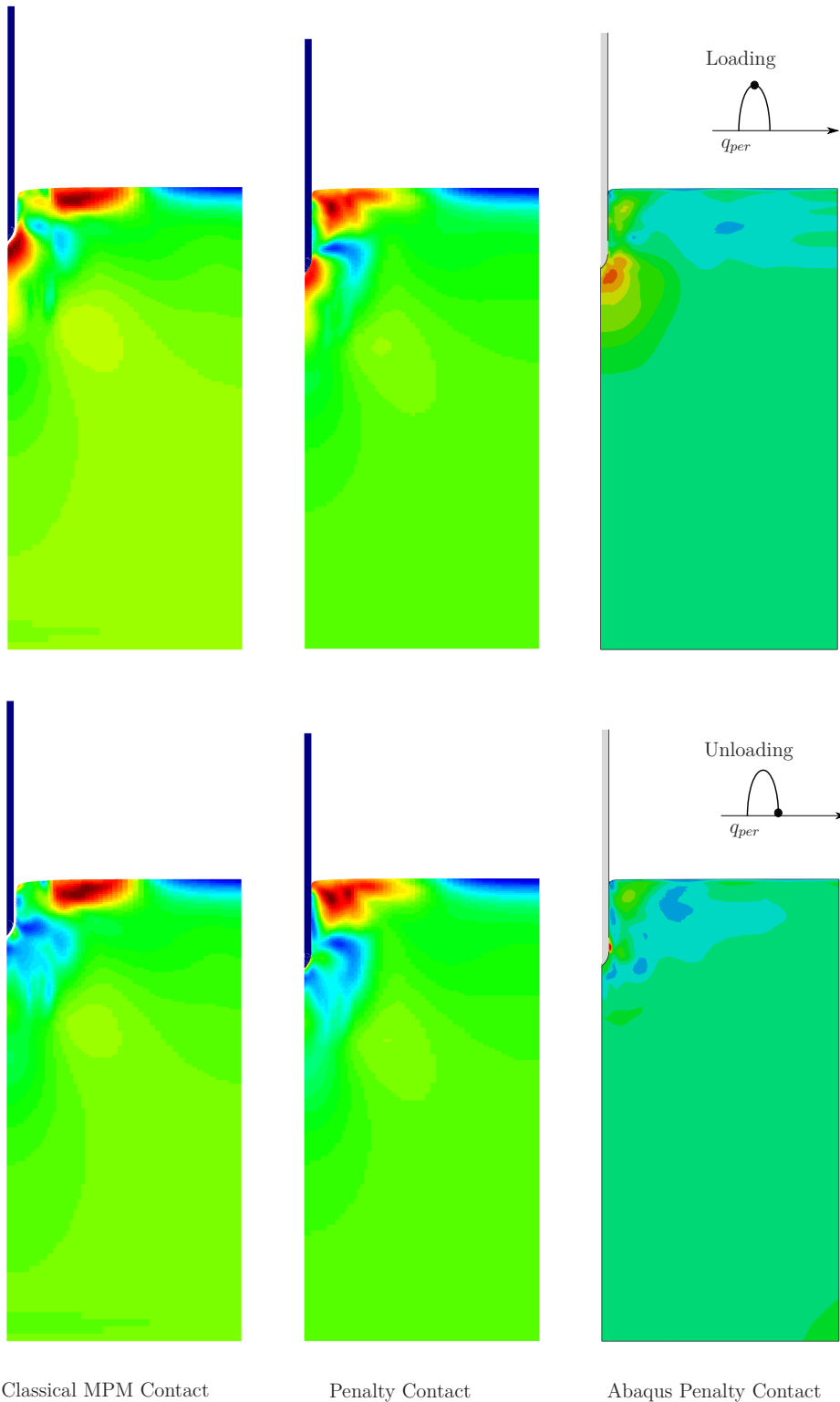
| Frictional MPM Contact | Penalty Contact | ABAQUS Penalty Contact |

Figure 4.5: Vertical stress comparison after gravity loading ; blue represents value of -170 kN/m^2

After obtaining the gravity stresses, the pile is hammered into the soil by activating the dynamic traction load q_{per} (see Figure 4.2). Due to high shear resistance along the pile shaft, the particle domains are heavily distorted in this region. Inspite of the hypoplastic model being developed upon the Matsuoka-Nakai criterion, a clearly defined failure surface is not obtained. Alternatively, the mobilised friction angle, a state variable in the hypoplastic sand model can be considered as an equivalent to the failure criterion. This corresponds to an upper limit of the critical friction angle ϕ_c. One region where failure is observed is under the pile which is highly compressed. It is observed that some material points exceed the critical angle of 30°, but most of these regions return back to the unloaded state within 0.05sec. Furthermore, non-homogenous variation of friction angles in the soil beneath the pile is observed. This is due the stress waves bouncing off the rigid boundary. This is more pronounced in material models dependent on stress levels, such as present case. Figure 4.6 depicts the mobilised friction angle during one blow of loading and unloading.

Figure 4.6: Friction angle comparison in loading-unloading of one blow ; blue represents zero, and red represents a value of 40°

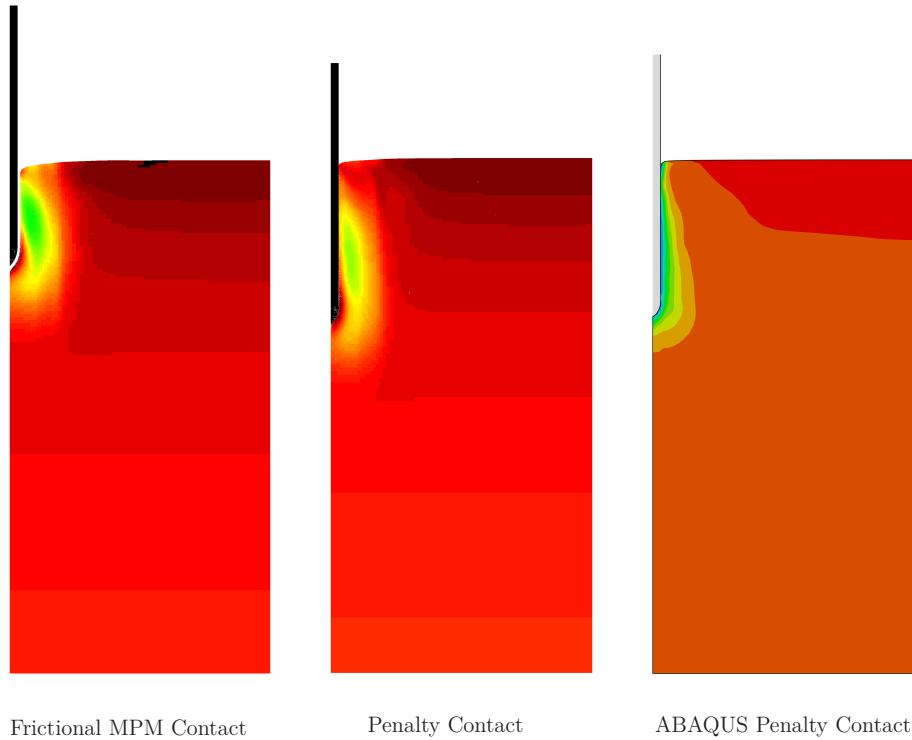| Frictional MPM Contact | Penalty Contact | ABAQUS Penalty Contact |

Figure 4.7: Void ratio comparison ; blue corresponds to a void ratio of 0.35 and red represents the initial value of 0.65

Another crucial part of simulating the installation process is the soil-pile interaction, especially in the case where the material exhibits high non-linearity. Incorporation of hypoplastic model shows that influence of predicting the volume change in the soil is limited to narrow zone close to the pile [2]. From Figrue 4.5, it is evident that the stresses are distributed in the vicinity of the pile, supporting the applicability of the contact algorithm that has been implemented in this work.

Due to the initial dense state of the soil, there is dilation around the pile due to high shear stresses. During the oscillatory movement of the pile during the dynamic loading phase, the zone near to the pile is heavily densified. From a practical view, the size of the influence zone in the case of classical MPM contact is overpredicted. To improve the result, a finer discretisation can be made around the shaft of the pile where high shear stresses occur. This comes at a increased computation and storage cost. These noises are attributed to the MPM contact and is more visible because of the high variation in stiffness between the interacting bodies. In case of the penalty contact, this variation in distribution of void ratio is more smooth. This is attributed to reduced noises in the contact algorithm due to the proposed mapping procedure of the contact forces to the computational grid, and provides a weighted average of the interface forces, eventually producing fairly smooth contact stresses. Results obtained from ABAQUS is also comparable to that obtained from the penalty contact algorithm (see Figure 4.7).
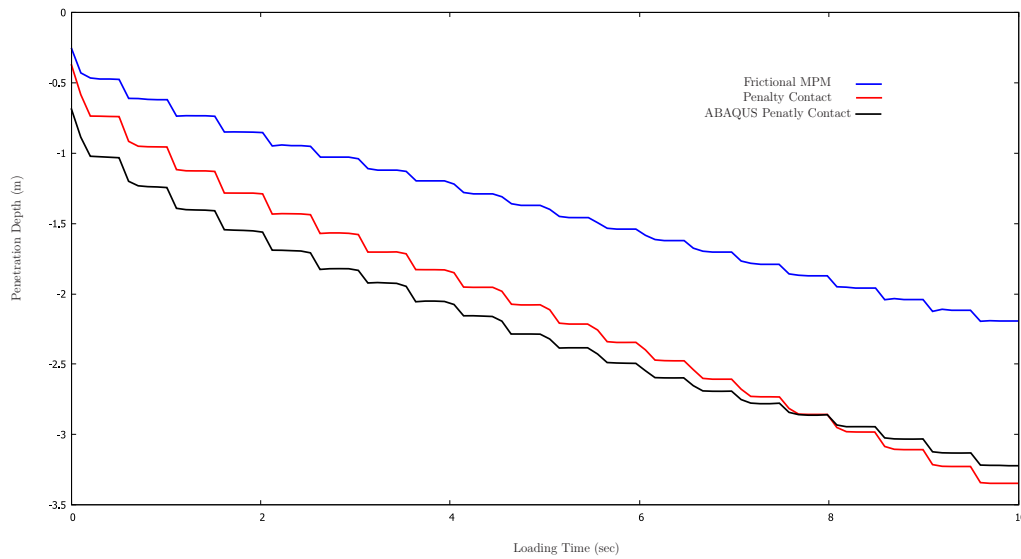
Figure 4.8: Depth of penetration of pile during dynamic loading stage

Another results that is discussed is the depth of penetration of pile in the three cases of frictional MPM contact, the penalty contact and the ABAQUS penalty contact simulations (see Figure 4.8) during the dynamic loading stage. It is evident that the results obtained from the proposed penalty contact algorithm are in agreement to a similar simulation performed in ABAQUS. A penetration of depth of 3.3m is obtained in the case of both ABAQUS simulation and Penalty MPM contact algorithm, as opposed to a penetration depth of 2.2m in the case of frictional contact algorithm. In the formulation of frictional MPM contact, the detection of material points's interaction is initiated within the influence of one computational grid. The resistance force is therefore overestimated, thereby yielding lower penetration depth. In the case of penalty contact however, resisting contact forces are established in three steps. Once it is confirmed that different discretisations contribute to the same computational node, elements attached to this node are tagged as those that can potentially be in contact. Between these elements, the search algorithm checks whether the slave node penetrates into the master segment, and once this is confirmed, a resisting force proportional to the depth of penetration is evaluated. The contact forces are mapped from the one-dimensional boundary mesh to the four-node computational mesh. This ensures that the resisting force is not overestimated, and the results obtained Figure 4.8 also suggests that the same.

Finally, a comparison of radial and axial stresses after 10 blows and 20 blows of the pile between the frictional contact algorithm, the penalty contact and the ABAQUS simulation is depicted via contour plots in Figures 4.9 and 4.10. It is inferred from the results that the penalty contact algorithm yields results more close to those obtained from ABAQUS simulation, than the frictional contact algorithm.

After 10 blows

After 20 blows

Frictional Contact   Penalty Contact   ABAQUS Penalty Contact
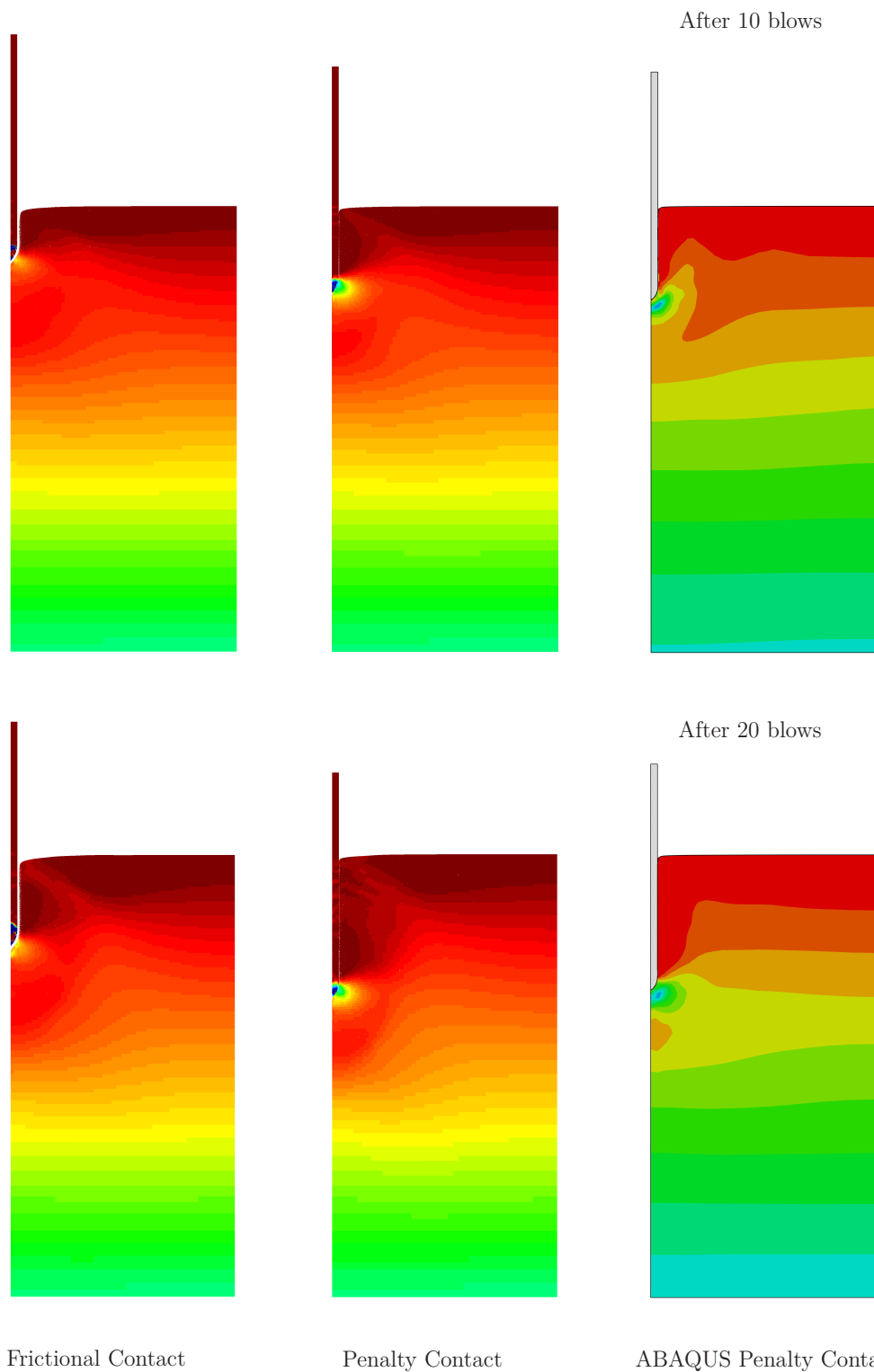
Figure 4.9: Radial stress comparison ; blue corresponds to a value of -120 kN/m^2

After 10 blows

After 20 blows

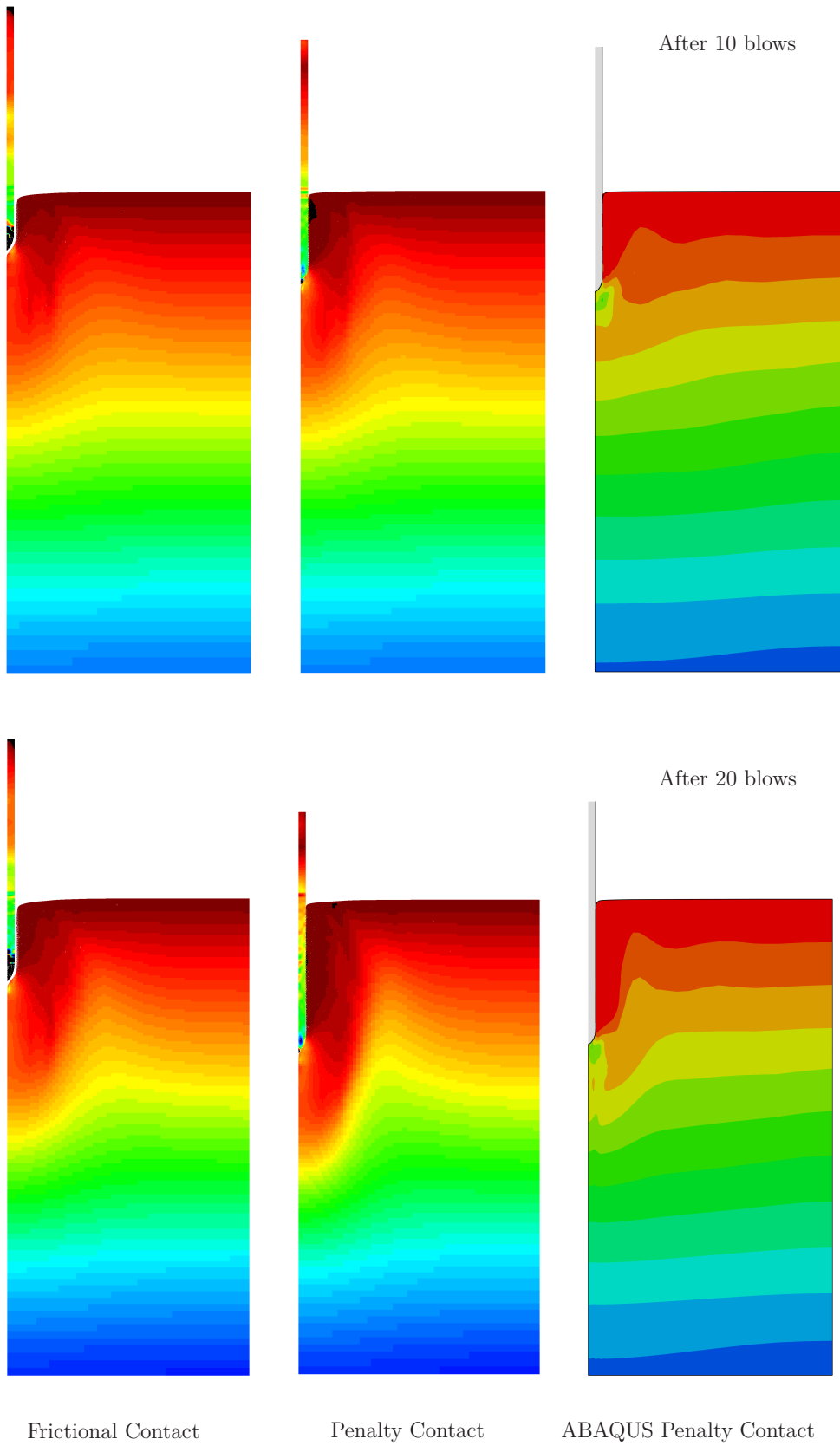Frictional Contact   Penalty Contact   ABAQUS Penalty Contact

Figure 4.10: Vertical stress comparison ; blue corresponds to a value of -170 kN/m^2

Chapter 5

Summary of the Thesis and Future work

The concluding remarks made in this chapter is with respect to the work described in this Thesis. As the title of the Thesis suggests, the work focussed on improving the present frictional contact algorithm for betterment of analysis using the Material Point Method.

In the scheme implemented in the work, the penalty function method is reformulated in the framework of CPDI, an improvement over MPM. The surface of the continuum is discretised separately from the MPM so that contact between different entities can be performed accurately. This is achieved by discretising the interface elements with two-node linear segments. A minuscule thickness is also assigned to the surface so that mass is allocated to the surface nodes according to the density of the continuum. Bookkeeping of the surface nodes is separated from the material points database. The penalty function method is then applied on this interface surface to evaluate the contact forces between two entities. The coupling between the background computational discretisation and the interface mesh is achieved by adding the contact forces as an external force to the momentum equation. The numerical formulation of CPDI and the Penalty contact is presented in Chapter 2.

In Chapter 3, the numerical formulation of hypoplastic soil model following von Wolffersdorff [65] is presented. It's extension to small-strain stiffness to account for intergranular strain is present along with the constrained modulus calculation, which is required to calculate the wavespeed, and ultimately, the size of the critical time step in CPDI setting. An biaxial element test of the constitutive model is performed in a finite element program and is compared with the results obtained from a Commerical finite element package, PLAXIS, in order to evaluate the applicability of the soil model for further simulations, and the results obtained are comparable.

With the contact algorithm proposed in Chapter 2, a pile installation problem is simulated and the results are compared with simulations using a classical MPM contact, as well as a simulation carried out in a commercial finite element package ABAQUS. Here, the results from the pile installation simulation are compared and it is evident that the proposed penalty contact algorithm estimates the behaviour much closer to the ABAQUS results than the classical MPM contact. The penetration depth which the proposed penalty contact algorithm outperforms the frictional contact algorithm, the friction angle is also compared as an equivalent to the failure criterion. Void ratios from the simulations are also presented

to monitor the densification of soil during the during loading process. The results indicate that the penalty contact is more comparable to ABAQUS simulation than the frictional MPM contact. Finally, the penetration depth during the dynamic loading stage of all the simulations are presented and the results suggests the the penalty contact yields closer results to the ABAQUS simulation.

Future work will investigate the use of rigid contact between the pile and the soil body. Implementing this method would eliminate the need for material point discretisation within the pile. This would assist in reducing the computational cost of the simulation. Future work would also dwell on simulating pile installation in an soil using hypoplastic clay material model. Pile installation in an undrained soil condition is also of interest as it would simulate more closely the offshore conditions.

Appendix A

Continuum Mechanics

A.1 Continuum Mechanics

We define an initial reference configuration of a continuous body Ω_0 enclosed with a boundary Γ_0 at time t_0 in a reference configuration. The body is subjected to a motion and as a result, the body deforms to the current configuration Ω with a boundary Γ corresponding to time t. The position of a certain point belonging to the reference configuration is defined by $\mathbf{X}$, whereas $\mathbf{x}$ denotes the position in the current configuration. Due to the motion, the displacement of the field can be traced giving the two deformation configurations as shown in Figure A.1.

A.1.1 Displacement Field

The displacement field of a particle relates its position in the undeformed configuration to its position in the deformed configuration. This is denoted by

$$\boldsymbol{u}\left(\boldsymbol{x},t\right) = \boldsymbol{x}\left(\boldsymbol{X},t\right) - \boldsymbol{X}, \tag{A.1}$$

where, $\boldsymbol{u}$ is the displacement vector. It is represented in index notation as u_i with $i \in (1,2,3)$, time $t \in [t_0, t_f]$, with t_0 and t_f being the initial and final time, respectively. An alternate definition is provided for the displacement if the deformed configuration $\boldsymbol{x}$ is the independent variable instead of the reference configuration $\boldsymbol{X}$.

A.1.2 Velocity and acceleration field

In solid mechanics, the motion and the deformation of a continuum body are described in terms of the displacement field. Primary field quantities describing the kinematic properties can be the velocity field and the acceleration field as well. Velocity v is defined as the rate of change of position vector for a material point. Acceleration is defined as the second derivative of the displacement vector. Applying the above definitions to Equation A.1 and using the chain rule of differentiation, we obtain the following vectors

$$\frac{du_i}{dt} = v_i, \qquad \frac{dv_i\left(x_i,t\right)}{dt} = \frac{\partial v_i}{\partial t} + v_j\frac{\partial x_i}{\partial x_j}, \tag{A.2}$$

where d implies the substantial derivative consisting of both the local and convective term. In case of updated Lagrangian formulation, the last term is neglected as the material deformation is tracked. There is therefore no distinction between the derivatives with respect to $\boldsymbol{X}$ or $\boldsymbol{x}$.
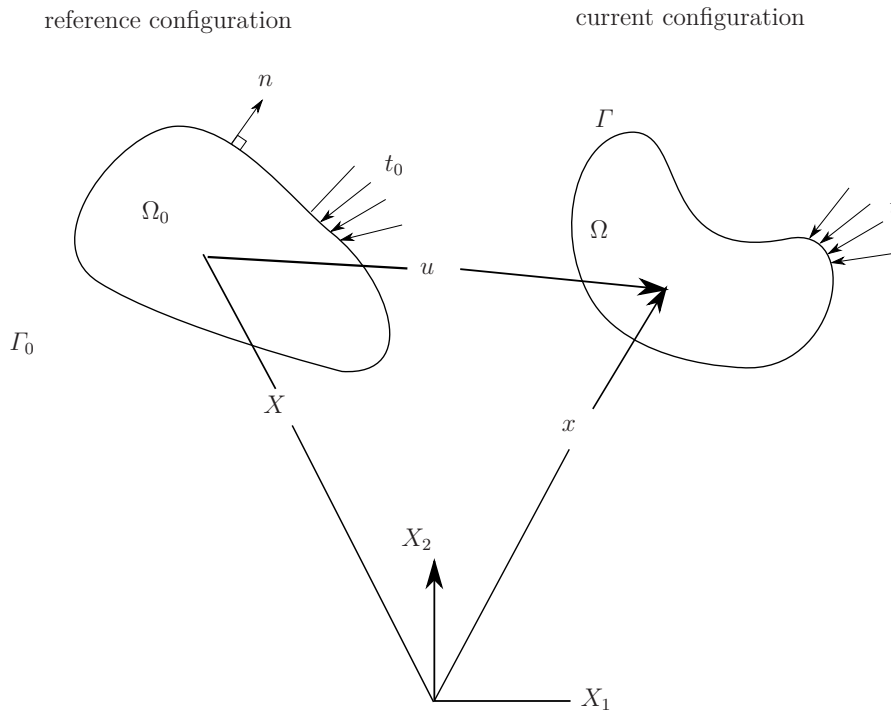
Figure A.1: Configuration of a continuum body

A.1.3 Strain

The strain ϵ_{ij} is a second order tensor and is defined as the normalised deformation with respect to a reference length. It is easier to represent the strain tensor in a vector form exploiting the property of symmetry of the strain tensor. It is represented as

$$\boldsymbol{\epsilon} = \begin{bmatrix} \epsilon_{11} & \epsilon_{22} & \epsilon_{33} & 2\epsilon_{12} & 2\epsilon_{23} & 2\epsilon_{13} \end{bmatrix}^T, \tag{A.3}$$

where, the vector in Equation A.3 contains the total strain components. For material modelling, a rate form of strain is usually considered $\dot{\boldsymbol{\epsilon}}$. It is given as the symmetrical part of the velocity gradient, depicted as

$$\epsilon_{ij} = \frac{1}{2} \left(\frac{\partial v_i}{\partial x_j} + \frac{\partial v_j}{\partial x_i} \right). \tag{A.4}$$

The strain is either recognised as Lagrangian or Eulerian, depending on whether it is based on the reference or the current configuration, respectively. For a rigid body motion, it is clear that there must be no strain in the system, if otherwise leads to development of stress.

A.1.4 Stress

Stress develops through a continuum as a result of deformation. Stress applied on the current configuration is characterised by the Cauchy stress tensor. The stress tensor is

represented as

$$\boldsymbol{\sigma} = \begin{bmatrix} \sigma_{11} & \sigma_{12} & \sigma_{13} \\ \sigma_{21} & \sigma_{22} & \sigma_{23} \\ \sigma_{31} & \sigma_{32} & \sigma_{33} \end{bmatrix}. \tag{A.5}$$

Cauchy stress tensor is symmetric, and therefore has six independent stress components acting at a certain point in the body. It can be represented in a vector form as well exploiting its symmetry and is given by

$$\boldsymbol{\sigma}\left(\boldsymbol{x}, t\right) = \begin{bmatrix} \sigma_{11} & \sigma_{22} & \sigma_{33} & \sigma_{12} & \sigma_{23} & \sigma_{13} \end{bmatrix}^{T}. \tag{A.6}$$

Cauchy stress is also regarded as the true stress as it refers to the deformed configuration.

Bibliography

[1] Issam J Al-Kafaji. *Formulation of a dynamic material point method (MPM) for geomechanical problems.* PhD thesis, Institute of Geotechnical Engineering, University of Stuttgart, 2013.

[2] M Arnold and I Herle. Hypoplastic description of the frictional behaviour of contacts. *Numerical methods in geotechnical engineering*, Taylor & Francis, London:101–106, 2006.

[3] SW Attaway, MW Heinstein, and JW Swegle. Coupling of smooth particle hydrodynamics with the finite element method. *Nuclear engineering and design*, 150(2): 199–205, 1994.

[4] SG Bardenhagen and JU Brackbill. Dynamic stress bridging in granular material. *Journal of Applied Physics*, 83(11):5732–5740, 1998.

[5] SG Bardenhagen and EM Kober. The generalized interpolation material point method. *CMES: Computer Modeling in Engineering & Sciences*, 5(6):477–495, 2004.

[6] S.G. Bardenhagen, J.U. Brackbill, and D.L. Sulsky. Shear deformation in granular material. In *11th International Detonation Symposium*, 1998.

[7] S.G. Bardenhagen, J.U. Brackbill, and D. Sulsky. The material–point method for granular materials. *Computer Methods in Applied Mechanics and Engineering*, 187 (3–4):529–541, 2000.

[8] S.G. Bardenhagen, J.E. Guilkey, K.M. Roessig, J.U. Brackbill, W.M. Witzel, and J.C. Foster. An improved contact algorithm for the material point method and application to stress propagation in granular material. *CMES: Computer Modeling in Engineering & Sciences*, 2(4):509–522, 2001.

[9] Ted Belytschko, Yun Yun Lu, and Lei Gu. Element-free galerkin methods. *International journal for numerical methods in engineering*, 37(2):229–256, 1994.

[10] L Beuth, Z Więckowski, and PA Vermeer. Solution of quasi–static large–strain problems by the material point method. *International Journal for Numerical and Analytical Methods in Geomechanics*, 35(13):1451–1465, 2011.

[11] Lars Beuth, Thomas Benz, Pieter A Vermeer, and Zdzisław Więckowski. Large deformation analysis using a quasi-static material point method. 2008.

[12] Jeremiah U Brackbill, Douglas B Kothe, and Hans M Ruppel. FLIP: A low-dissipation, particle–in–cell method for fluid flow. *Computer Physics Communications*, 48(1):25–38, 1988.

[13] JU Brackbill and HM Ruppel. FLIP: A method for adaptively zoned, particle–in–cell calculations of fluid flows in two dimensions. *Journal of Computational Physics*, 65(2): 314–343, 1986.

[14] Oscar Buneman. Dissipation of currents in ionized media. *Physical Review*, 115(3): 503, 1959.

[15] D Burgess, D Sulsky, and JU Brackbill. Mass matrix formulation of the FLIP particle–in–cell method. *Journal of Computational Physics*, 103(1):1–15, 1992.

[16] CJ Coetzee. *The modelling of granular flow using the particle-in-cell method*. PhD thesis, Department of Mechanical Engineering, University of Stellenbosch, Stellenbosch, South Africa, 2004.

[17] SJ Cummins and JU Brackbill. An implicit particle-in-cell method for granular materials. *Journal of Computational Physics*, 180(2):506–548, 2002.

[18] John Dawson. One-dimensional plasma model. *Physics of Fluids (1958-1988)*, 5(4): 445–459, 1962.

[19] J. Donea, A. Huerta, J.Ph. Ponthot, and A. Rodríguez-Ferran. Arbitrary Lagrangian–Eulerian methods. *Encyclopedia of Computational Mechanics*, 2004.

[20] JN Franzius, DM Potts, and JB Burland. The influence of soil anisotropy and k 0 on ground surface movements resulting from tunnel excavation. *Géotechnique*, 55(3): 189–199, 2005.

[21] J.E. Guilkey, J.B. Hoying, and J.A. Weiss. Computational modeling of multicellular constructs with the material point method. *Journal of Biomechanics*, 39(11):2074–2086, 2006.

[22] Fursan Hamad. *Formulation of a dynamic material point method and applications to soil–water–geotextile systems*. PhD thesis, Institute of Geotechnical Engineering, University of Stuttgart, 2014.

[23] Fursan Hamad. Formulation of the axisymmetric CPDI with application to pile driving in sand. *Computers and Geotechnics*, 74:141–150, 2016.

[24] Francis H Harlow. Hydrodynamic problems involving large fluid distortions. *Journal of the ACM (JACM)*, 4(2):137–142, 1957.

[25] Francis H Harlow. The particle-in-cell computing method for fluid dynamics. *Methods in Computational Physics*, 3:319–343, 1964.

[26] S Henke. Influence of pile installation on adjacent structures. *International journal for numerical and analytical methods in geomechanics*, 34(11):1191–1210, 2010.

[27] S. Henke and J. Grabe. Simulation of pile driving by 3–dimensional Finite-Element analysis. In *Proceedings of the 17th European Young Geotechnical Engineers Conference, Zagreb*, pages 215–233, 2006.

[28] I Herle and D Kolymbas. Hypoplasticity for soils with low friction angles. *Computers and Geotechnics*, 31(5):365–373, 2004.

[29] Michael A Homel, Rebecca M Brannon, and James Guilkey. Simulation of shaped–charge jet penetration into drained and undrained sandstone using the material point method with new approaches for constitutive modeling. In *11th World Congress on Computational Mechanics (WCCM XI), Barcelona, Spain*, pages 676–687, 2014.

[30] W Hu and Z Chen. A multi–mesh MPM for simulating the meshing process of spur gears. *Computers & Structures*, 81(20):1991–2002, 2003.

[31] GR Johnson and RA Stryk. Conversion of 3d distorted element method for hypervelocity impact simulation. *Int. J. Impact Eng*, 28:947–966, 2003.

[32] Nam-Ho Kim. *Introduction to nonlinear finite element analysis*. Springer Science & Business Media, 2014.

[33] Nam Ho Kim, Young Ho Park, and Kyung Kook Choi. Optimization of a hyper-elastic structure with multibody contact using continuum-based shape design sensitivity analysis. *Structural and multidisciplinary optimization*, 21(3):196–208, 2001.

[34] SL Lee, YK Chow, GP Karunaratne, and KY Wong. Rational wave equation model for pile-driving analysis. *Journal of Geotechnical Engineering*, 114(3):306–325, 1988.

[35] YP Lian, X Zhang, and Y Liu. Coupling of finite element method with material point method by local multi–mesh contact method. *Computer Methods in Applied Mechanics and Engineering*, 200(47):3482–3494, 2011.

[36] YP Lian, X Zhang, and Y Liu. An adaptive finite element material point method and its application in extreme deformation problems. *Computer Methods in Applied Mechanics and Engineering*, 241:275–285, 2012.

[37] L Lim, A Andreykiv, and RBJ Brinkgreve. On the application of the material point method for offshore foundations. *Numerical methods geotechnical engineering. Taylor and Francis Group, London*, pages 253–258, 2014.

[38] LJ Lim, A Andreykiv, and RBJ Brinkgreve. Pile penetration simulation with material point method. *Installation Effects in Geotechnical Engineering*, pages 24–30, 2012.

[39] E Love and DL Sulsky. An unconditionally stable, energy–momentum consistent implementation of the material-point method. *Computer Methods in Applied Mechanics and Engineering*, 195(33):3903–3925, 2006.

[40] Leon B Lucy. A numerical approach to the testing of the fission hypothesis. *The Astronomical Journal*, 82(12):1013–1024, 1977.

[41] J Ma, D Wang, and MF Randolph. A new contact algorithm in the material point method for geotechnical simulations. *International Journal for Numerical and Analytical Methods in Geomechanics*, 38(11):1197–1210, 2014.

[42] ZT Ma, X Zhang, and P Huang. An object–oriented MPM framework for simulation of large deformation and contact of numerous grains. *Computer Modeling in Engineering and Sciences (CMES)*, 55(1):61–88, 2010.

[43] Mounir E Mabsout and John L Tassoulas. A finite element model for the simulation of pile driving. *International Journal for numerical methods in Engineering*, 37(2): 257–278, 1994.

[44] D Mašín. A hypoplastic constitutive model for clays. *International Journal for Numerical and Analytical Methods in Geomechanics*, 29(4):311–336, 2005.

[45] John A Nairn and James E Guilkey. Axisymmetric form of the generalized interpolation material point method. *International Journal for Numerical Methods in Engineering*, 101(2):127–147, 2015.

[46] M Nazem, JP Carter, and DW Airey. Arbitrary Lagrangian–Eulerian method for dynamic analysis of geotechnical problems. *Computers and Geotechnics*, 36(4):549–557, 2009.

[47] A Niemunis and I Herle. Hypoplastic model for cohesionless soils with elastic strain range. *Mechanics of Cohesive-frictional Materials*, 2(4):279–299, 1997.

[48] Andrzej Niemunis. *Extended hypoplastic models for soils*, volume 34. Inst. für Grundbau und Bodenmechanik, 2003.

[49] Andrzej Niemunis, Carlos Eduardo Grandas-Tavera, and Luis Felipe Prada-Sarmiento. Anisotropic visco-hypoplasticity. *Acta Geotechnica*, 4(4):293–314, 2009.

[50] A Nishiguchi and T Yabe. Second-order fluid particle scheme. *Journal of Computational Physics*, 52(2):390–413, 1983.

[51] Eugenio Oñate, Sergio R Idelsohn, Facundo Del Pin, and Romain Aubry. The particle finite element method—an overview. *International Journal of Computational Methods*, 1(02):267–307, 2004.

[52] Jens Pfister and Peter Eberhard. Frictional contact of flexible and rigid bodies. *Granular Matter*, 4(1):25–36, 2002.

[53] Gang Qiu, Sascha Henke, and Jürgen Grabe. Application of a coupled Eulerian–Lagrangian approach on geomechanical problems involving large deformations. *Computers and Geotechnics*, 38(1):30–39, 2011.

[54] MF Randolph. Science and empiricism in pile foundation design. *Geotechnique*, 53 (10):847–876, 2003.

[55] A Sadeghirad, RM Brannon, and J Burghardt. A convected particle domain interpolation technique to extend applicability of the material point method for problems involving massive deformations. *International Journal for Numerical Methods in Engineering*, 86(12):1435–1456, 2011.

[56] A Sadeghirad, RM Brannon, and JE Guilkey. Second-order convected particle domain interpolation (CPDI2) with enrichment for weak discontinuities at material interfaces. *International Journal for Numerical Methods in Engineering*, 95(11):928–952, 2013.

[57] IM Smith and YK Chow. Three dimensional analysis of pile drivability. In *Proc. 2nd Int. Conf. on Numerical Methods in Offshore Piling, Austin, Texas*, pages 1–19, 1982.

[58] D Sulsky and A Kaul. Implicit dynamics in the material-point method. *Computer Methods in Applied Mechanics and Engineering*, 193(12):1137–1170, 2004.

[59] D. Sulsky and H. Schreyer. The particle–in–cell method as a natural impact algorithm. *Advanced Computational Methods for Material Modeling, ASME, AMD*, 180:219–230, 1993.

[60] D Sulsky and HL Schreyer. A particle method with large rotations applied to the penetration of history–dependent materials. *Advances in Numerical Simulation Techniques for Penetration and Perforation of Solids, ASME, AMD*, 171:95–102, 1993.

[61] D. Sulsky and H.L. Shreyer. Axisymmetric form of the material point method with application to upsetting and Taylor impact problems. *Computer Methods in Applied Mechanics and Engineering*, 139(1):409–429, 1996.

[62] D Sulsky, SJ Zhou, and HL Schreyer. Application of a particle–in–cell method to solid mechanics. *Computer Physics Communications*, 87(1):236–252, 1995.

[63] Deborah Sulsky and JU Brackbill. A numerical method for suspension flow. *Journal of Computational Physics*, 96(2):339–368, 1991.

[64] Deborah Sulsky, Zhen Chen, and Howard L Schreyer. A particle method for history–dependent materials. *Computer Methods in Applied Mechanics and Engineering*, 118 (1):179–196, 1994.

[65] P-A von Wolffersdorff. A hypoplastic relation for granular materials with a predefined limit state surface. *Mechanics of Cohesive-frictional Materials*, 1(3):251–271, 1996.

[66] T Weifner and D Kolymbas. A hypoplastic model for clay and sand. *Acta Geotechnica*, 2(2):103–112, 2007.

[67] Z Więckowski, SK Youn, and JH Yeon. A particle–in–cell solution to the silo discharging problem. *International Journal for Numerical Methods in Engineering*, 45 (9):1203–1225, 1999.

[68] Wei Wu and Erich Bauer. A simple hypoplastic constitutive model for sand. *International Journal for Numerical and Analytical Methods in Geomechanics*, 18(12): 833–862, 1994.

[69] Pan Xiao-Fei, Xu Ai-Guo, Zhang Guang-Cai, Zhang Ping, Zhu Jian-Shi, Ma Shang, and Zhang Xiong. Three–dimensional multi–mesh material point method for solving collision problems. *Communications in Theoretical Physics*, 49(5):1129, 2008.

[70] AR York. *The development of modifications to the material point method for the simulation of thin membranes, compressible fluids, and their interactions.* PhD thesis, The University of New Mexico, 1997.

[71] X Zhang, KY Sze, and S Ma. An explicit material point finite element method for hyper-velocity impact. *International Journal for Numerical Methods in Engineering*, 66(4):689–706, 2006.

[72] Yonggang Zheng, Fei Gao, Hongwu Zhang, and Mengkai Lu. Improved convected particle domain interpolation method for coupled dynamic analysis of fully saturated porous media involving large deformation. *Computer Methods in Applied Mechanics and Engineering*, 257:150–163, 2013.